npj | climate and atmospheric science

Article

Published in partnership with CECCR at King Abdulaziz University

https://doi.org/10.1038/s41612-025-01319-y

Projected changes in atmospheric pathways of Western North American heatwaves simulated from high-resolution coupled model simulations

Check for updates

Mingyu Park[1,2,3] ✉ & Nathaniel C. Johnson[2]

Western North America (WNA) is a regional hotspot for summer heat extremes. However, our understanding of the atmospheric processes driving WNA heatwaves remains largely based on a few case studies. In this study, we investigate the general characteristics of atmospheric pathways associated with WNA heatwaves using a 30-member high-resolution coupled model simulation. Synthesizing the WNA heatwave events across the large ensemble, we reinforce the view that WNA heatwaves are systematically driven by: (1) a Rossby wave train originating from the western North Pacific, (2) poleward moisture transport toward the Gulf of Alaska, occasionally via atmospheric rivers, and (3) downstream ridge amplification over WNA. Although these features also appear in the late twenty-first-century projections, notable changes include farther poleward moisture transport and broader ridge development in the future. Under the anomaly-based heatwave definition used in this study, which removes the influence of mean temperature change, the frequency of WNA heatwaves is projected to decrease. Our findings suggest that mechanisms identified in case studies, including upstream Rossby wave packets and subsequent moist processes, are broadly applicable to understanding WNA heatwaves over recent decades and their projected changes.

The year 2024 was recorded as the warmest year in the 175-year observational record, marking a 1.5 °C increase in global mean surface temperature compared to the pre-industrial level[1]. The global warming, further accelerated in recent decades, has been linked not only to an increasing trend in the frequency and intensity of summer heat extremes worldwide[2–4], but also to a higher probability of record-shattering magnitudes in these events[5–7]. The impacts of extreme heat events on socioeconomic losses and environmental damage are substantial, as demonstrated by observational findings on widespread heat-related mortality[8], crop yield sensitivity[9], increased wildfire activity[10], and disruptions to net ecosystem carbon uptake[11], all of which have drawn extensive attention from the scientific community. Regarding the overall frequency of temperature extremes, changes in the mean temperature of a given temperature distribution appear to play a leading role[5,6], a relationship that has been documented over recent decades in various observational datasets and is well simulated by climate models[12–14].

On a regional scale, however, dynamical atmospheric processes also play a significant role in regulating local temperature variability. The Pacific Northwest heatwave in June 2021 is a notable example, illustrating how synoptic-scale atmospheric circulation contributed to the development and persistence of heat extremes in that midlatitude location[15]. It was a record-breaking extreme heat event over North America[16,17], meteorologically characterized by an upstream extratropical cyclone with latent heat release and an amplified upper-level ridge over the Pacific Northwest. This synoptic condition led to an unprecedented surface temperature increase through the combined effect of upstream diabatic processes, adiabatic warming by subsidence, and enhanced clear-sky shortwave radiation[15,18–22]. Previous studies further showed that during this particular event, anomalously high moisture was transported in the form of a narrow and intense filament, identified as an atmospheric river[23,24], and that this synoptic-scale moisture transport could in turn be traced back to a Rossby wave train originating from the subtropical western North Pacific[24,25]. The sequence of an upstream

[1]Department of Geosciences, Program in Atmospheric and Oceanic Sciences, Princeton University, Princeton, NJ, USA. [2]Geophysical Fluid Dynamics Laboratory, National Oceanic and Atmospheric Administration, Princeton, NJ, USA. [3]Department of Civil Urban Earth and Environmental Engineering, Ulsan National Institute of Science and Technology, Ulsan, Republic of Korea. ✉e-mail: meteopark@unist.ac.kr

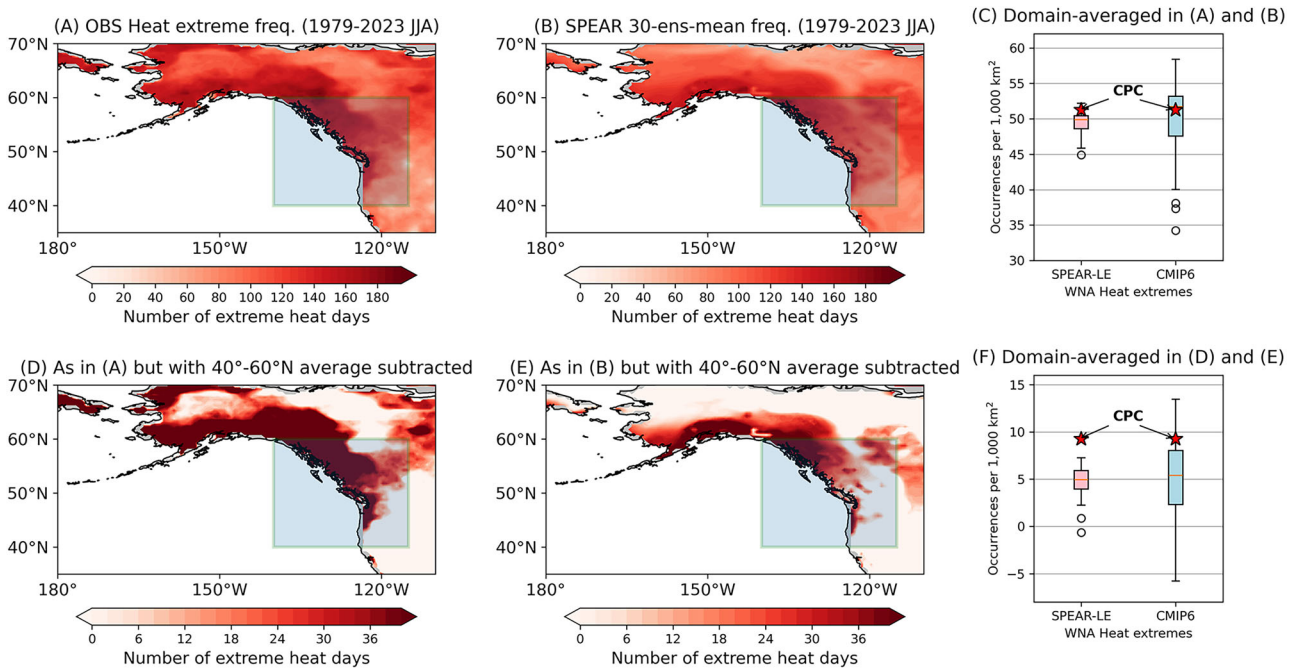

Fig. 1 | Comparison between observations and SPEAR in representing Western North America as a regional hotspot of boreal summer heat extremes. Occurrence of heat extremes over western North America (WNA) during the recent historical (1979–2023, June-July-August) period from **A** observed (CPC data) T_{max} and **B** SPEAR-MED T_{max} data. **C** Boxplots of WNA domain-averaged heat extreme occurrences from (**A**) and (**B**). In addition, statistics from 30 climate models (i.e., 29 CMIP6 models and the first SPEAR ensemble member; see Table S1 for the list of models) are included for comparison and shown in the right boxplot. The medians of the model ensemble spread are indicated by thin orange lines, while white circles represent outliers. The CPC value is indicated by a red star. **D**–**F** As in **A**–**C** but with the latitudinal average over 40°–60°N removed. In **F**, the CPC value is indicated by a red star. Green boxes in **A**, **B**, **D**, **E** denote the WNA domain used in this study, defined as 40°–60°N and 140°W–115°W.

Rossby wave packet, moisture transport, and a persistent anticyclonic circulation (i.e., atmospheric blocking), as observed in the 2021 Pacific Northwest heatwave, constitutes an atmospheric pathway for driving regional extreme heat events[26–28].

Our understanding of this atmospheric pathway during boreal summer heatwaves, particularly those over western North America (WNA), can be deepened by using recently developed large ensemble simulations. Due to the rare nature of extreme weather events, the enhancement of the sample sizes offered by climate model large ensembles provides a means for investigating significant circulation patterns and surface responses associated with WNA heatwaves. Such an analysis can help determine whether the atmospheric processes associated with WNA heatwaves exhibit a systematic pattern originating from farther upstream regions, and whether they can be generalized throughout their evolution. Furthermore, although atmospheric blocks intensified by upstream moist processes are typically observed within the oceanic storm track regions, including the North Pacific[29,30], their general linkage to WNA heatwaves and atmospheric moisture transport remains largely unexplored. This study therefore aims to identify a robust relationship between atmospheric processes and WNA heatwaves by utilizing the Seamless system for Prediction and Earth system Research Large Ensemble (SPEAR-LE; Method), recently developed at the Geophysical Fluid Dynamics Laboratory of the National Oceanic and Atmospheric Administration (NOAA). The advantages of using large ensembles to investigate extreme temperature events for both deriving robust statistics of their characteristics[6,7,16,31–34] and achieving a high signal-to-noise ratio in synoptic-scale atmospheric circulation responses[35–37] have been well demonstrated.

This study also aims to address how the atmospheric pathway associated with WNA heatwaves will respond to a warming climate. The case study of the Pacific Northwest event[18] suggested that the contribution of upstream moisture transport may become more significant in future heat extremes, given that saturation vapor pressure is expected to increase nonlinearly under a warming climate following the Clausius–Clapeyron relationship[38], enabling the increased amount of water vapor in the atmosphere. This thermodynamic change, reflected in projected increases in saturation specific humidity, plays a dominant role in the increasing trend of extreme precipitation in the midlatitudes[39]. However, it is still uncertain whether the response of WNA heatwaves becomes stronger in the projection, because atmospheric circulation associated with WNA heatwaves will also change simultaneously. In light of the above, we explore how atmospheric moisture transport and blocking associated with WNA heatwaves are reshaped in future emissions scenarios (i.e., SSP2-4.5 and SSP5-8.5). Throughout the study, we use high-resolution large-ensemble simulations with an atmospheric horizontal grid spacing of 50 km and an ocean horizontal grid spacing of nominal 1.0° (i.e., SPEAR-MED).

Results

Current and projected changes in the frequency of Western North American heat extremes

We begin by examining the frequency of heat extremes over WNA, further motivating the focus on the WNA region, and then investigating their projected changes under two different emissions scenarios. While various approaches exist to define heat extremes, we use an anomaly-based heatwave definition to effectively capture local temporal peaks that are strongly coupled with synoptic-scale atmospheric circulation variability. Specifically, to identify regional hotspots of heat extremes over land, we focus on short-term temperature variations beyond both high-frequency weather noise and the long-term mean warming. To this end, we remove the seasonal cycle and apply a 5-day moving average to daily maximum 2-meter temperatures (T_{max}) anomalies to isolate more persistent heat anomalies. We also remove the long-term trend to isolate variations beyond the mean warming (see Methods). Using this T_{max} anomaly field, we select days (i.e., the central day of the 5-day period) at each land grid point with T_{max} values that exceed 2.0 standard deviations of the June-July-August (JJA) values and define them as heat extremes. Figure 1 shows the spatial distribution of boreal summer heat extremes during the recent historical period (i.e., 1979–2023 JJA) in the

Climate Prediction Center (CPC) global unified temperature dataset, used as the observational reference, and SPEAR. Both datasets highlight the preferred locations of heatwave occurrences along the west coast of North America, including the Pacific Northwest. In terms of the median over the WNA domain (i.e., 40°–60°N, 140°–115°W; denoted by green boxes in Fig. 1), approximately 49.9 heat extreme occurrences per 1000 Km^2 are simulated by the 30 ensemble members of SPEAR (Fig. 1C). We also find that the observed heat extreme frequency averaged over the WNA domain (i.e., 51.2 occurrences per 1000 Km^2) lies within the model ensemble range and is approximately 2.6% higher than the ensemble mean.

The longitudinal variation in this heat extreme frequency from observation and model simulations becomes more pronounced when the zonally averaged frequency over the midlatitudes (i.e., 40°–60°N) is subtracted, as shown in Fig. 1D, E. However, in contrast to the raw values, the longitudinal variation simulated by SPEAR shows a systematic underestimation (Fig. 1F). In a later section, we show that this underestimation is potentially due to weaker amplitudes of North Pacific storm track and westerly jet stream intensity in the model. To compare SPEAR's performance with other climate models, we additionally used output from 29 Coupled Model Intercomparison Project Phase 6 (CMIP6)[40] models and computed WNA heatwave occurrences in the same manner (see Table S1 for the list of models used in this study). As a result, the boxplots of CMIP6 models in Fig. 1C, F show that the observed values are well captured by the CMIP6 intermodel spread, which is several times larger than the range from the SPEAR large ensemble simulations. Climate models also reproduce the overall spatial pattern of heat extreme occurrences, such as regional hotspots over western North America (Fig. S1). However, for zonal asymmetry, the interquartile range of CMIP6 models (Fig. 1F) does not include the CPC value, indicating that climate models tend to underestimate this metric. The similarity between the medians of the CMIP6 models and the SPEAR simulations (orange lines in the boxplots) suggests that SPEAR performs comparably to the average of the CMIP6 models used in this study. The statistics of individual models in Fig. S1 support that the SPEAR model shows moderately good performance in representing WNA heat extremes relative to other CMIP6 models. Based on these results, we conclude that SPEAR captures key observed aspects of WNA heat extremes and is a relevant modeling system for investigating projected changes.

With this result from both observations and SPEAR that WNA has experienced elevated frequencies of heat extremes relative to surrounding land areas during the historical period, we move onto the frequency of heat extremes in the SSP5-8.5 and SSP2-4.5 emissions scenarios (Fig. 2). We again apply the same criterion to define heat extremes but relative to this future period (i.e., 2056–2100 JJA; Methods). In both high and intermediate radiative forcing simulations, the medians of WNA heat extreme frequencies are approximately 44.8 and 46.7 occurrences per 1000 Km^2 (Fig. 2G), respectively, substantially lower than during the historical period (Fig. 2B, C). This decrease in the frequency of WNA heat extreme occurrences depends on the removal of the mean temperature increase effect in computing the T_{max} anomaly in the future period, which is equivalent to shifting the baseline of temperature distribution. If the same historical base period is applied to T_{max} in future projections, the number of WNA heat extremes would be considerably increased relative to that of the historical period[7,41]. However, from the framework adopted in this study, which removes the mean temperature increase, the dynamic and thermodynamic processes that induce extreme temperature anomalies over WNA may weaken under global warming. Moreover, the simulated zonally asymmetric features in heat extreme frequency (Fig. 2E, F) become much weaker, except for the coastal regions where the impact of marine heatwaves dominates[42]. This reduced asymmetry is also detectable from the projected decrease in the standard deviation and skewness of the T_{max} anomaly distribution over WNA (Fig. S2). The reductions shown in Fig. 2 primarily reflect the reduction in skewness, given that we define heat extremes using standard deviation thresholds that are unique to each period.

The warming rate of extreme hot days in certain regions notably deviates from the summer mean warming rate[13,41,43,44], due to the contribution from regional drivers of temperature variability. Indeed, previous studies showed that some regions, including WNA, actually exhibit projected decreases in temperature anomalies and heatwave frequency after the removal of mean warming effects[41,45], as supported by Fig. 2. In this context, we aim to further investigate whether this decrease is causally linked to changes in regional atmospheric circulation[46–48] in the following sections. Since temperature extremes in the SPEAR SSP2-4.5 scenario are spatially consistent with those in the SSP5-8.5 scenario but exhibit a generally weaker rate of increase[7,34], we hereafter show model results from the SSP5-8.5 scenario only.

Evolution of atmospheric circulation and moisture transport during Western North American heatwaves

We next investigate the spatiotemporal evolution of atmospheric processes related to WNA heatwaves. Earlier studies have examined the statistics and metrics by aggregating mid-latitude land grid points to provide a theoretical understanding[17,49] and to compare the relative importance of physical processes responsible for heat extremes[6,11,50]. Others have employed grid point-based temperatures or domain-averaged indices to analyze temporal extrema and long-term trends[7,13,16,44,48,51]. However, if one focuses on heatwaves within a certain region, it should be considered that the size and location of regional heat extremes are unique in every case, particularly when regulated by daily atmospheric circulation anomalies.

Taking this into account, we introduce a methodology to identify a sizeable extreme heat event over WNA (see "Methods" for a detailed description). We first filter a T_{max} anomaly field over land by the 2.0 standard deviation threshold, calculated from all JJA days at each grid point, as in Fig. 1. Next, an object tracking algorithm[52] with a size threshold of 10^6 Km^2 is applied to this filtered T_{max} anomaly field to isolate large, continuous regions ("blobs") that meet the heat extreme threshold. Any blob that has a center of mass (i.e., the mean location of T_{max} anomalies within the blob) being located within the WNA domain is defined as a WNA heatwave event. This procedure has been illustrated in Fig. S3 for a particular heatwave event in a single ensemble member. For the following lag composite analysis, we only take onset days of the WNA heatwave events into account, which corresponds to lag 0 in the composites, and composite T_{max}, 500-hPa geopotential height (Z500), and vertically integrated water vapor fluxes (IVT; Methods) from each ensemble member.

Figure 3 shows the ensemble averaged results associated with the evolution of WNA heatwaves during the recent historical and future periods. A hint on the development of a Rossby wave train over the North Pacific is clearly seen by the Z500 anomaly field (i.e., black contours in Fig. 3A), indicating that this upstream atmospheric circulation can be simulated earlier than a week prior to the onset of WNA heatwave, while there is no signal of T_{max} anomaly in the WNA domain (i.e., purple box in Fig. 3). Note that the simulated spatial structure of the upstream circulation anomaly resembles that of the 2021 Pacific Northwest event[19,23,24]. Also, the trough centered over the Sea of Okhotsk begins to bring moisture to the central North Pacific where a weak ridge is situated. The Rossby wave train pattern becomes distinct at the following pentad of lag days −7 to −3 (Fig. 3B) and comprises cyclonic circulation anomalies over the Far East Asia, anticyclonic circulation anomalies centered at the west of the dateline, and cyclonic circulation anomalies over the central to eastern North Pacific Ocean. Together with the atmospheric ridge situated over WNA, anomalous moisture flux (i.e., denoted by green vectors) develops and propagates poleward along the western flank of this ridge. Previous studies of atmospheric blocking have shown that this upstream moisture transport leads to the amplification of downstream blocking[29,53–56], suggesting that this moist process may have contributed to the growth of an atmospheric ridge during WNA heatwave events.

In Fig. 3C, T_{max} anomalies reach the peak in the WNA domain, corresponding to the WNA heatwave definition, accompanied by intense anticyclonic circulation anomalies. As will be shown later, these quasi-stationary upper-level ridges simulated by SPEAR are often identified as atmospheric blocks, consistent with the typically observed relation between

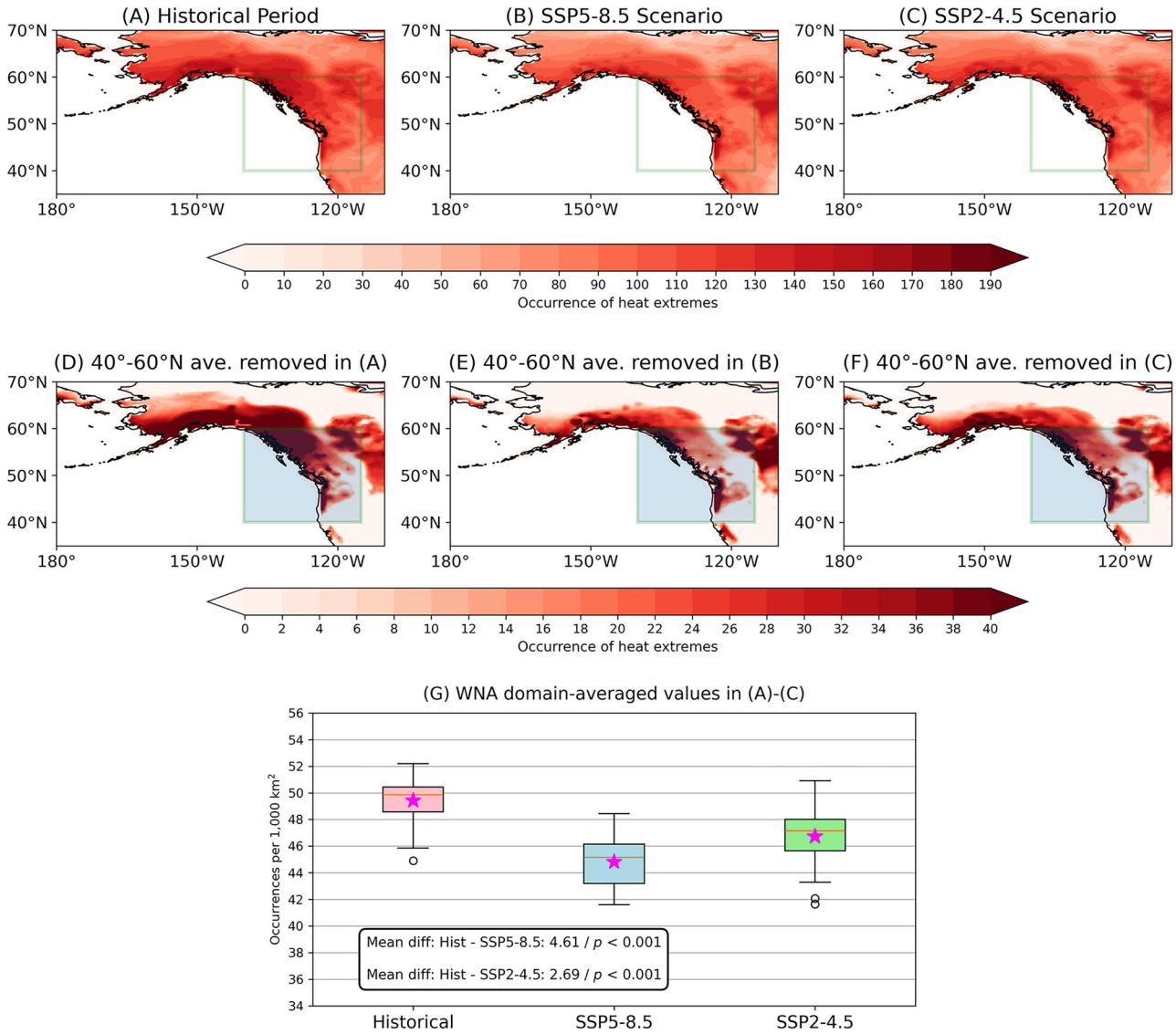

Fig. 2 | Western North America as a regional hotspot of boreal summer heat extremes. Occurrence of heat extremes over western North America (WNA) during **A** the recent historical (1979–2023, June-July-August) and **B**, **C** late twenty-first century (2056–2100, June-July-August) periods under the **B** SSP5-8.5 and **C** SSP2-4.5 scenarios, expressed as the number of occurrences over the analyzed period. **D**–**F** As in **A**–**C** but with the zonal average over 40°–60°N removed. **G** Boxplots of WNA domain-averaged heat extreme occurrences for all periods and scenarios. The mean and median of the model ensemble spread are indicated by a pink star and a thin red line, respectively, while white circles represent outliers. The statistical tests of the mean differences between the historical and future periods are shown at the bottom of the panel, evaluated using Welch's *t*-test. Green boxes in **A**–**F** denote the WNA subdomain used in this study.

blocking and heatwaves[26,27,57]. It is also notable that moisture transport toward WNA is blocked by atmospheric flow but diverted toward northern Canada, which thus exacerbates dry surface conditions locally. Across eastern North America, on the other hand, negative T_{max} anomalies with an atmospheric trough concurrently develop, resulting in a zonal dipole structure of T_{max} over North America. In accordance with the dissipation of the upstream Rossby wave train and associated moisture transport, these continental-scale temperature anomalies substantially weaken in lag days +3 to +7 (Fig. 3D), which is followed by a termination of the heatwave and blocking over WNA.

In the late twenty-first century period, although the growth and decay of T_{max} and Z500 anomalies are generally similar to that in the recent historical period, some notable differences are found at each pentad. For example, during the period between approximately 1 and 2 weeks preceding the WNA heatwave (Fig. 3E), the circulation response over East Asia and the North Pacific is not as pronounced as that in the recent historical period. This slower development of the wave train leads to weaker magnitudes of the trough-ridge-trough upstream pattern in the following pentad (Fig. 3F). However, we also see a farther poleward moisture transport along with a broader extent of anticyclonic flow over WNA, which persists and intensifies until the peak of WNA heatwaves (Fig. 3G). Accordingly, a broader region undergoes positive T_{max} anomalies during WNA heatwave events in the future projection.

In short, the overall characteristics of atmospheric physical processes associated with heatwaves are similar in both recent historical and late projection periods. The general sequence is: (1) a Rossby wave train generated from the western North Pacific, (2) poleward moisture transport along a trough over the central North Pacific, and (3) amplification of the anticyclonic circulation anomaly over WNA. However, there are some notable differences between the two periods, such as moisture anomalies transported farther poleward and a broader atmospheric ridge development in the latter period. Therefore, with this qualitative picture of heatwave evolution in mind, we proceed to investigate how atmospheric physical processes are spatially linked to the WNA heatwaves and what structural changes between them are projected to occur in the future.

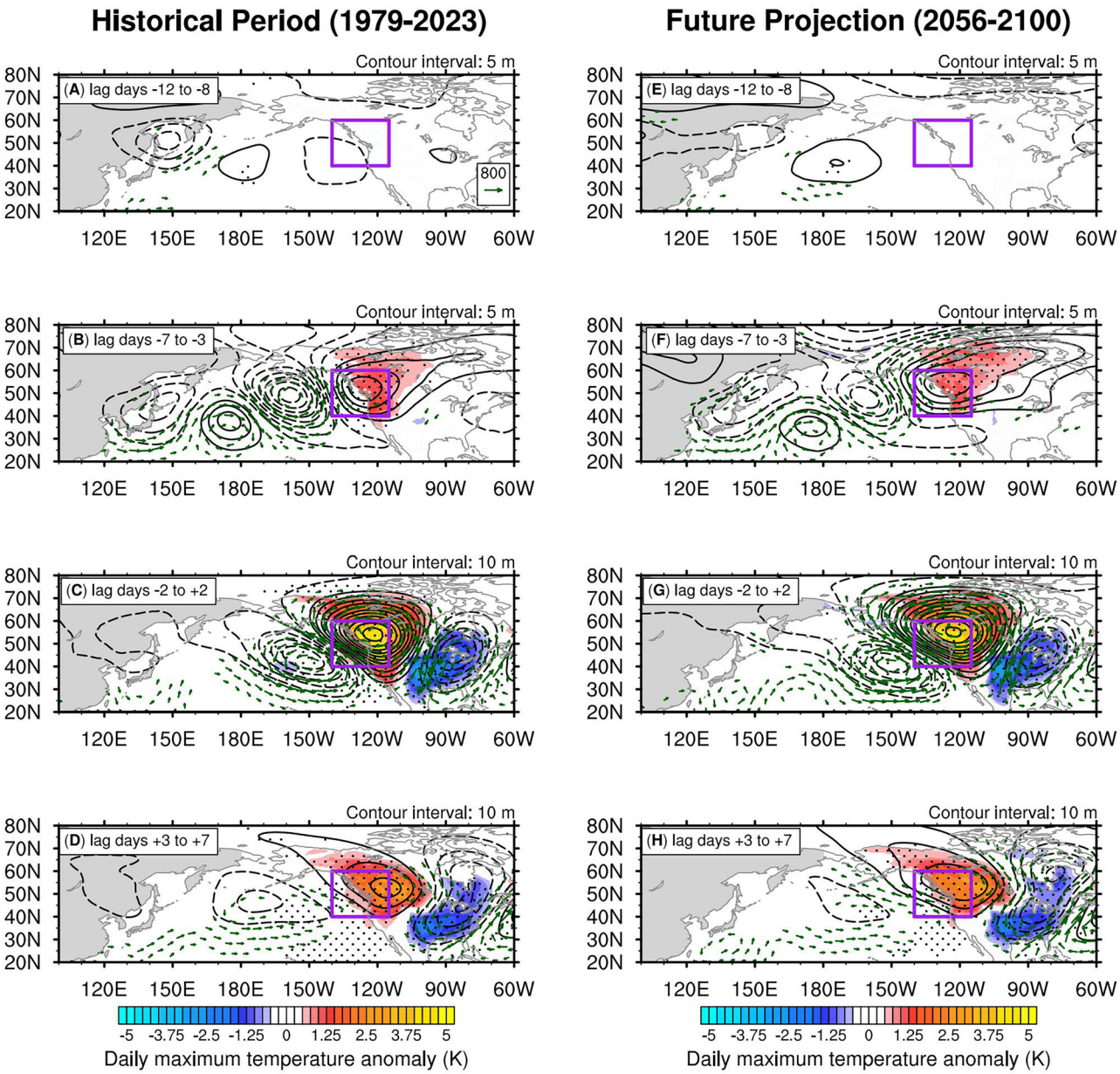

Fig. 3 | Simulated evolution of Western North American heatwaves and associated atmospheric processes over the North Pacific Ocean. A–D Pentad composites of T_{max} anomaly (shading; K) and 500-hPa geopotential height anomaly (Z500; black contour; m), and vertically integrated moisture flux (IVT; green vector; $kgm^{-1}\ s^{-1}$) averaged over **A** lag days −12 to −8, **B** −7 to −3, **C** −2 to +2, and **D** +3 to +7 during WNA heatwaves from the recent historical SPEAR simulations. Lag day 0 corresponds to the onset day of WNA heatwaves. **E–H** As in **A–D** but during late twenty-first century WNA heatwaves under SSP5-8.5. Stippling indicates a region where at least 80% of ensemble members agree with the sign of anomaly. Contour interval of Z500 field is denoted at the upper right corner of each panel. For visualization, IVT vectors smaller than 200 kg $m^{-1}\ s^{-1}$ are not shown.

Projected changes in moisture transport, atmospheric river, and atmospheric blocking associated with Western North American heatwaves

In this subsection, we employ a heatwave-centered diagnostic approach, analogous to the atmospheric blocking-centered diagnostics[29,35,58], to quantitatively investigate the projected changes of linkages between WNA heatwaves and associated physical drivers. This method composites variables of interest with respect to the center of all WNA heatwaves (i.e., 1,610 events in the historical period and 1,450 events in the late twenty-first century period; Fig. S4) onto coordinates defined by relative longitude and latitude.

The first row in Fig. 4 exhibits the T_{max} anomalies composited against the center of WNA heatwaves (pink dots in Fig. 4A, B) during the recent historical and late twenty-first century epochs. As expected, the area where the T_{max} anomalies are most intense is located around the heatwave center in both epochs. However, the peak intensity of WNA heatwaves in the projection becomes weaker than that of the historical period. To ascertain whether the properties of WNA heatwaves are projected to change significantly between the two periods, we further compared the distribution of their size and intensity (Fig. S4). Regarding the intensity, defined as the area-weighted average of T_{max} anomalies that exceed 2.0 standard deviations (i.e., heat extremes) in the identified heatwave, SPEAR simulates a significant heatwave weakening under the future emissions scenario, resulting in 0.44 K mean decrease ($p < 0.001$). In addition, the size of WNA heatwaves, defined as the area occupied by the identified WNA heatwave, decreases as well, with an average decrease of approximately 0.058 Mm^2 ($p < 0.001$). These results pose a question of whether atmospheric processes associated with WNA heatwaves show similar features such as a weakened intensity and reduced spatial extent under a future emissions scenario.

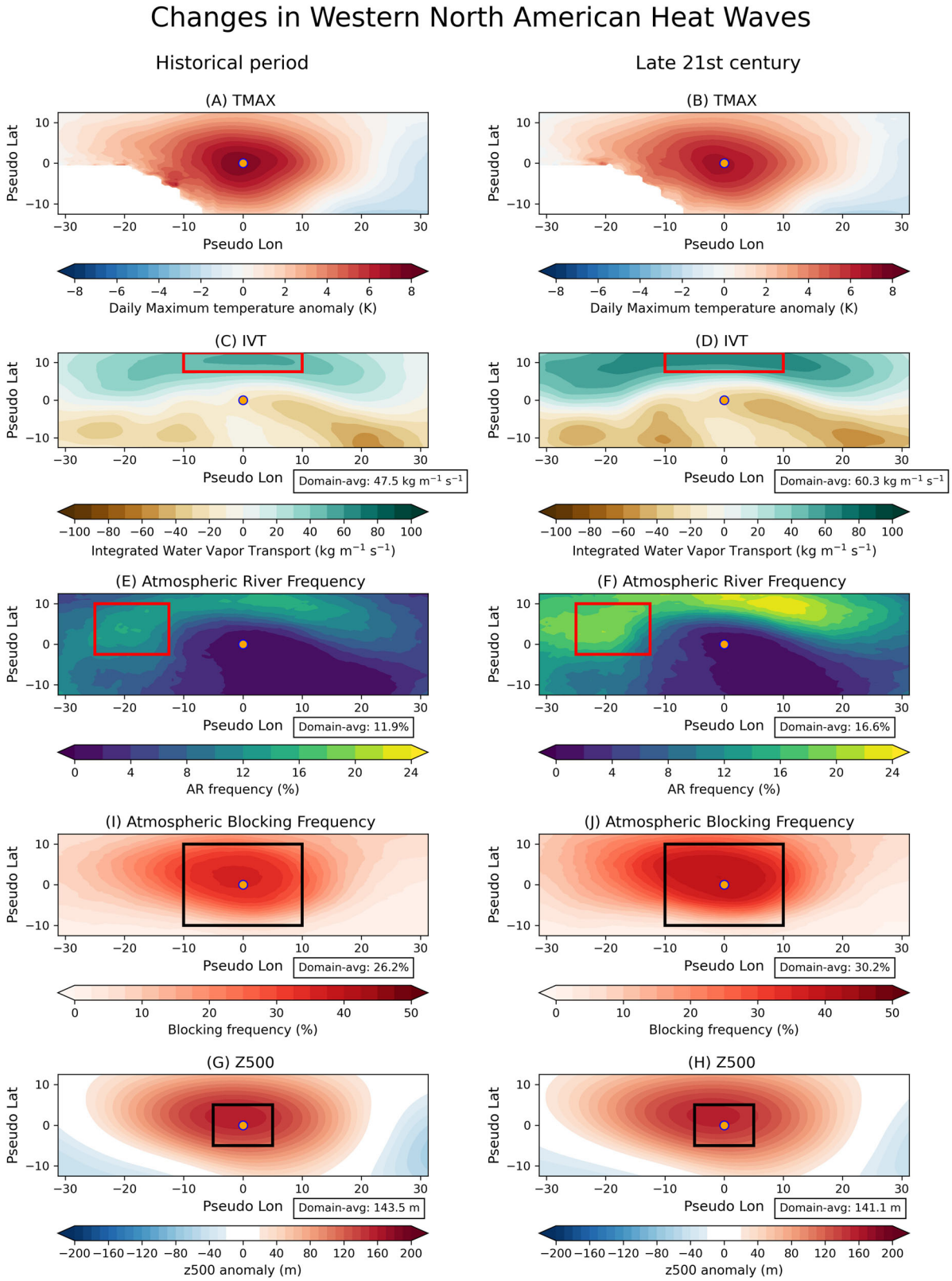

Fig. 4 | Spatial pattern of atmospheric processes during Western North American heatwave events. Heatwave-centered composites of **A**, **B** T_{max} anomalies over land (K), **C**, **D** IVT anomalies (kg m^{-1} s^{-1}), **E**, **F** atmospheric river frequency (%), **G**, **H** atmospheric blocking frequency (%), and **I**, **J** Z500 anomalies (m) during (left) the recent historical period and (right) late twenty-first century period under SSP5-8.5. In **A**, **B**, for visualization, T_{max} anomalies were spatially smoothed by two iterations of a nine-point smoothing. **C**–**J** Red and black boxes indicate the domains used to compute the domain-averaged values shown in the bottom right corner.

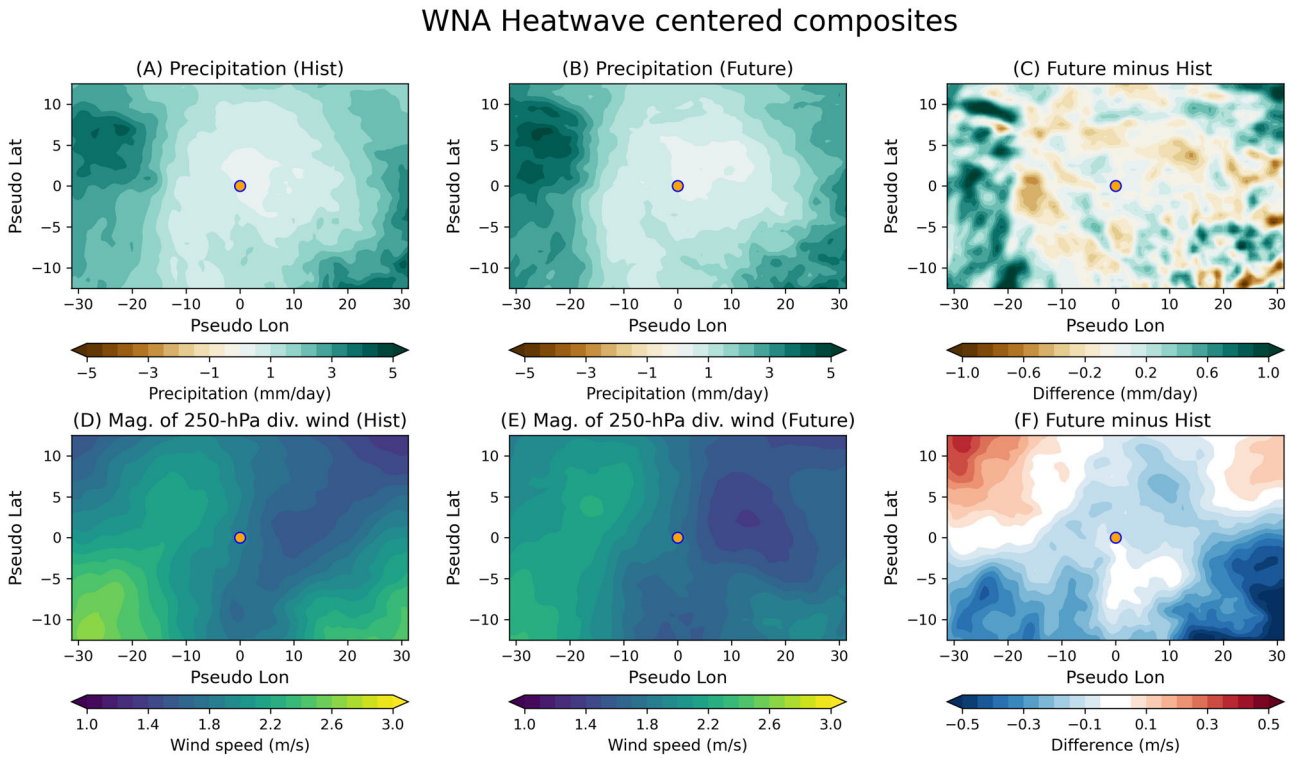

Fig. 5 | Spatial pattern of daily precipitation anomaly and 250-hPa divergent wind magnitudes during Western North American heatwave events. Heatwave-centered composites of **A**–**C** precipitation anomalies (mm day^{-1}) and **D**–**F** magnitude of 250-hPa divergent wind speed (m s^{-1}) during (left) the recent historical period and (center) late twenty-first century period under SSP5-8.5, and (right) their differences.

To address the above question, we next examine the composites of vertically integrated moisture transport in the same manner. During the recent historical period, positive IVT anomalies are situated at the poleward flank of the heatwave center (Fig. 4C), indicating poleward moisture transport, consistent with the direction of moisture flux in Fig. 3. In the later epoch, however, moisture transport by circulation anomalies around WNA is strengthened and becomes more extensive (Fig. 4D), due to the increased availability of moisture during boreal summer in a warming climate[35,59], despite the weaker magnitudes of the upstream Rossby wave train (Fig. 3F). Motivated by the importance of atmospheric rivers for temperature extremes over WNA[23,24,60], as discussed in the introduction, we further examine the frequency of atmospheric rivers associated with the simulated moisture transport. The projected enhancement of moisture transport is similarly supported by the composite field of atmospheric river frequency (i.e., the fraction of atmospheric river occurrences during heatwaves) which shows a secondary peak on the western flank of heatwave events (Fig. 4E, F). This upstream maximum of atmospheric river frequency, shown in both periods, reflects that intense moisture transport and associated moist processes generally operate ahead of the WNA anticyclonic circulation pattern, consistent with the previous studies of the 2021 Pacific Northwest heatwave[18,19,23,24]. The local maximum becomes further pronounced when the heatwave-centered composites are constructed against the onset days of WNA heatwaves only (Fig. S5).

In line with the enhanced and broader moisture transport, the composited atmospheric blocking frequency (i.e., the fraction of occurrences of atmospheric blocking to heatwaves) shows a similar spatial response (Fig. 4G, H) under a warming climate. Again, a larger area of WNA heatwave events accompanies an increased fraction of co-occurrence of quasi-stationary and persistent atmospheric blocking events during the late twenty-first century period, compared to the recent historical period, particularly at the northwestern side of the heatwave center. While this northwestward expansion is also detectable in the Z500 field (Fig. 4H), there is no hint of increase in the projected peak intensity. Together with a reduction in the intensity of collocated T_{max} anomalies (Fig. 4B), the result rather suggests that the blocking intensity close to the center of heatwaves mildly weakens. The description of the aforementioned key features is further supported by domain-averaged quantities over the selected regions in Fig. 4.

Our results suggest that the projected increase in upstream moisture contributes to an expansion of blocking size over the western North American domain, but not to a strengthening of the block-center intensity. This weaker block intensity may seem counterintuitive given earlier studies highlighting the role of moist processes in blocking amplification[29,53]. In short, the proposed mechanism can be summarized as the following steps: (1) Positive moisture advection by cyclonic circulation → (2) latent heat release upstream of the blocking → (3) stronger ascent and subsequent divergent wind (i.e., divergent outflow produced by diabatic processes) → (4) greater negative potential vorticity (PV) advection by the divergent outflow (i.e., $v_{\chi} \cdot \nabla PV$) at upper levels. While the first step of the mechanism, greater moisture advection by cyclonic circulation, is explicitly shown by Fig. 4, whether the remaining processes operate has not been explicitly investigated. Unfortunately, the limited set of variables and coarse vertical resolution of the saved variables due to storage constraints from these large ensemble simulations restricts our ability to perform a detailed investigation of moist processes related to atmospheric blocking.

Despite these limitations, we further investigate whether (1) upstream latent heating is enhanced, and (2) the magnitude of divergent upper tropospheric wind is strengthened during future WNA heatwaves, using precipitation (as an estimate of latent heating) and horizontal wind. The first two rows of Fig. 5 show the heatwave-centered composites of precipitation anomalies and divergent wind amplitudes during the two different periods, composited against the center of WNA heatwaves. At the upstream region, consistent with the greater moisture transport and atmospheric river frequency in future projections (Fig. 4C–F), greater precipitation anomalies are found (Fig. 5A–C). However, the intensity of the divergent wind field southwest of the heatwave center, near the North Pacific storm track exit

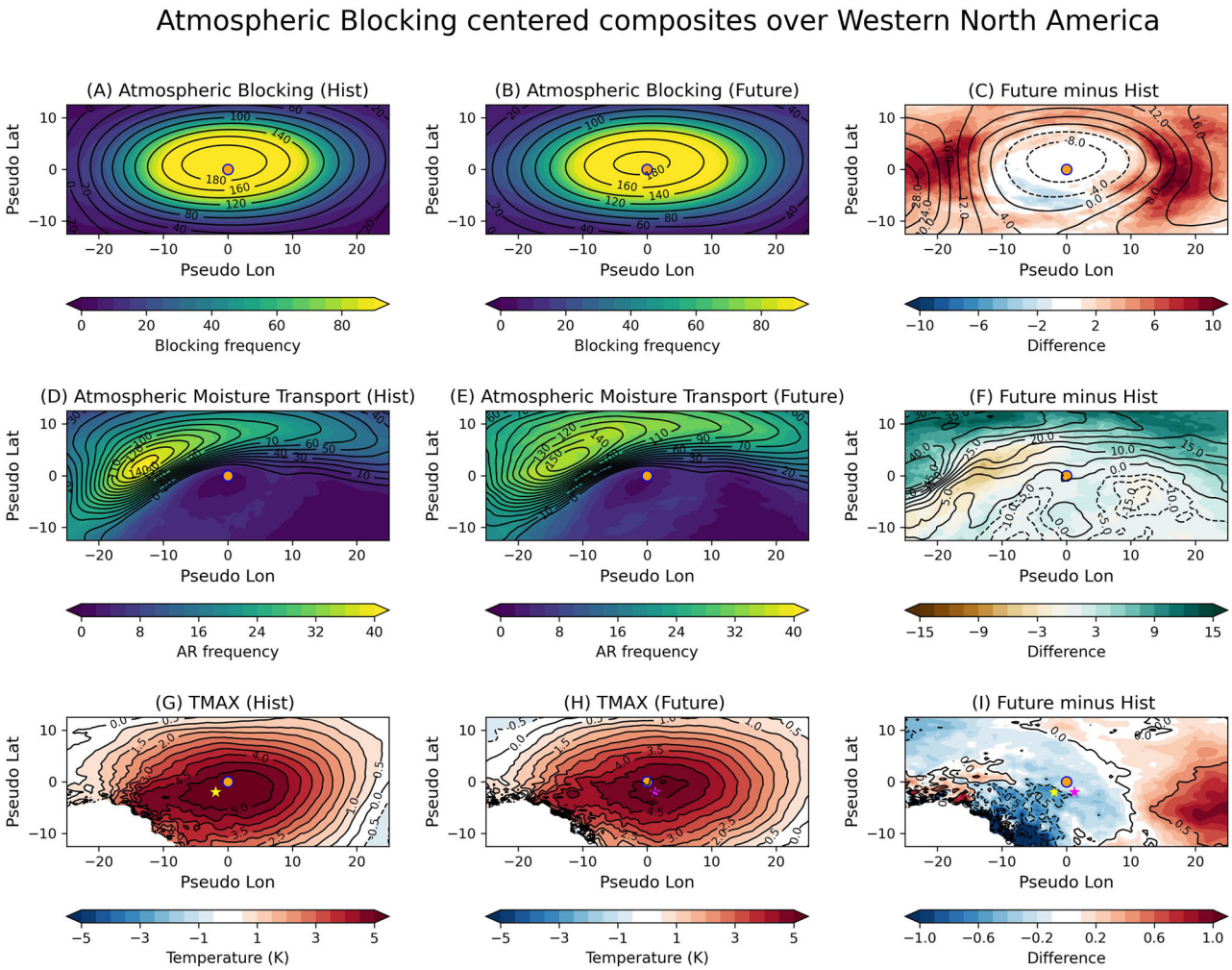

Fig. 6 | Spatial pattern of daily maximum temperature anomaly and atmospheric moisture transport during Western North American blocking events. Blocking-centered composites of **A**–**C** atmospheric blocking frequency (shading; %) and Z500 anomalies (black contours; m), **D**–**F** atmospheric river frequency (shading; %) and IVT anomalies (black contours; kg m^{-1} s^{-1}), and **G**–**I** T_{max} anomalies over land (shading; K) for the (left) recent historical period, (middle) late twenty-first century period under SSP5-8.5, and (right) differences between the two periods. Black contours in **A**, **B** indicate Z500 anomalies with an interval of 20 m, while those in **C** represents Z500 differences with an interval of 4 m. Black contours in **D**, **E** indicate IVT anomalies with an interval of 10 kg m^{-1} s^{-1}, while those in **F** represent IVT differences with an interval of 5 kg m^{-1} s^{-1}. Black contours in **G**–**I** outline T_{max} anomalies with an interval of 0.5 K. Yellow and purple stars indicate the location of peak T_{max} intensity during the recent historical and late twenty-first century periods, respectively.

region, is projected to weaken. In contrast, the divergent wind strengthens northwest of the heatwave center, consistent with a broader blocking pattern in the future period (e.g., Fig. 4H). Although the PV advection associated with divergent outflow, following previous studies, cannot be explicitly computed in this study due to data limitations, we infer that projected changes in the divergent wind do not effectively enhance downstream blocking intensity but rather contribute to an expansion of blocking size during WNA heatwave events.

The heatwave-centered plots in Fig. 4 reveal two important structural changes of atmospheric processes associated with WNA heatwaves under a future emissions scenario: First, a broader and stronger propagation of vertically integrated moisture flux is found in the proximity of the heatwave center. Second, the fraction of atmospheric blocking frequency increases with an increased width of WNA anticyclonic circulation anomalies. Whilst we do not attempt to address the causality between these changes in this study, it is worth noting that the importance of upstream diabatic processes on the ridge amplification over WNA, suggested by the earlier studies of blocking from the *global* perspective[29,30,35], is similarly found; during WNA heatwaves, a northeastward expansion of poleward moisture transport likely leads to a broadening of the ridge in the same direction through diabatic processes, rather than to an intensification of peak blocking intensity. To support that changes in the atmospheric processes affect the properties of WNA heatwaves, we shift our attention to atmospheric blocking over WNA to examine regional heatwaves from the viewpoint of atmospheric blocking.

Projected changes in Western North American blocking and their linkages to moisture transport and heatwaves

The blocking-centered composites for the two different periods, constructed in the same manner as the heatwave-centered composites, clearly show that the response of WNA blocking frequency is overall positive and concentrated on the western and eastern side of the blocking center (Fig. 6A–C). This increase in size of WNA blocks, which can be categorized into mid-latitude land blocks during boreal summer, is consistent with the earlier finding that blocks in general are projected to increase in size under a warming climate[59]. The corresponding composites of IVT and AR frequency show similar results in the sense that the poleward and eastward moisture transport by WNA anticyclonic circulation expands spatially and with greater intensity (Fig. 6D–F). However, we also note that a mild decrease of AR frequency approximately 15° longitude ahead of the blocking center (Fig. 6F) may have contributed to the weaker circulation amplitudes near the center through reduced diabatic effects. Namely, the location where upstream moist process of WNA blocking operates is likely to be displaced

farther westward and poleward in projections, as similarly shown by the precipitation differences during WNA heatwaves (Fig. 5C). This shift may imply a stronger positive feedback of moist processes on the outer region of the blocking compared to the historical period.

The decreased peak intensity of blocking over WNA captured from both blocking and heatwave-centered composites supports the aforementioned idea that the decreased temperature response close to the center of WNA heatwaves may have been induced by a weaker amplitude of circulation anomaly and thereby weaker dynamic warming. Indeed, we see that the T_{max} composites with respect to the blocking center display a similar response, with suppressed warming around the core of the blocks, particularly at the western flank where a weaker anticyclonic flow develops as indicated by the coarser Z500 gradients during the late twenty-first century period (Fig. 6C, D). The T_{max} response instead shows enhanced warming on the eastern flank of the blocking center, farther inland, in conjunction with the increased blocking frequency (Fig. 6C) and reduced moisture transport (Fig. 6F). This dipole structure of T_{max} changes is consistent with a recent CMIP6 modeling study showing projected changes in 2-m temperature anomalies associated with atmospheric ridges over the Pacific-American region[58], indicating that this temperature response in SPEAR is not model-specific. Our findings therefore highlight that the intensity and spatial extent of WNA heatwaves under a future emissions scenario are likely to be regulated by the projected changes in atmospheric processes such as upstream moisture transport and atmospheric blocking.

Whilst we mostly focused on the investigation of WNA heatwaves that substantially grow and decay in the intraseasonal time scale, as observed in the 2021 Pacific Northwest heatwave, the relationship between atmospheric circulation and regional heat extremes can also vary on the interannual time scale under a future emissions scenario. For instance, a recent study showed that some regions such as Europe and Greenland are projected to have significant changes in the heatwave-blocking relation that affect the overall frequency of heatwaves, besides the dominant effects of mean temperature increase[45]. Prompted by this finding, we have examined if a similar change in the heatwave-blocking relation is simulated over WNA (Fig. S6) by using the warm spell duration index[61] (Methods) that provides a large enough sample size to investigate the interannual variability of heatwaves (but includes those with a milder intensity), as in ref. 45. A comparison of the heatwave-blocking relationship between the two epochs, estimated by correlation between WNA heatwaves and blocking during the corresponding periods, shows only an insignificantly weak decrease in the relationship across ensemble members in the future projection. This relatively stable relationship suggests that the mean decrease in WNA heatwaves is, overall, proportional to the mean decrease in blocking frequency, once the contribution from mean temperature increase is excluded.

This study primarily focuses on projected changes in the atmospheric pathway that drives western North America heatwaves, but we do not rule out the possible contributions from significant changes in land properties (e.g., soil moisture) and related land-atmosphere interaction through the modulation of local evapotranspiration[62]. Indeed, a recent study suggested potential regime shifts in soil moisture-evaporation coupling across many regions under a warming climate[63], although little evidence of significant change is found over WNA in large ensemble simulations[44]. A more detailed exploration of this land-atmosphere coupling is beyond the scope of this study due to the unavailability of the required variables saved from the SPEAR simulations. Nonetheless, we emphasize the need for future research to understand how projected land-atmosphere coupling contribute to changes in the characteristics of WNA heatwaves and interacts with atmospheric processes[50,64].

Projected changes in the intensity of North Pacific atmospheric circulation and westerly jet stream in SPEAR

So far, we have examined the projected decrease in the frequency of WNA heatwave occurrences and the associated atmospheric processes using two different center-based composite approaches. At this point, one may ask whether projected changes in the mean state of the atmospheric circulation play a role in the weaker synoptic-scale wave train over the North Pacific during WNA heatwave events. In this subsection, we briefly address this question and provide further insights by examining the general characteristics of boreal summer circulation in the future projection.

We first demonstrate if this general weakening is similarly found from geopotential height eddy fields simulated by SPEAR. Figure 7 shows the 75th percentile of Z500 eddy field within the 40°–80°N latitudinal band, which serves as an indicator of the amplitude of midlatitude anticyclonic eddies. The result reveals that the mean value of SPEAR large ensemble during the historical period (i.e., approximately 61.5 m) is comparable to values obtained from various GFDL model configurations and the two reanalysis datasets used in a previous study[65]. Under SSP5-8.5, however, this mean value is projected to decrease by 1.5 m. This result therefore supports the notion that zonal eddies of the Northern Hemisphere during boreal summer generally become weaker under a warming climate. In fact, weakening of the boreal summer midlatitude circulation in future projections has been robustly simulated in climate models[66]. For instance, recent storm track studies have consistently shown projected weakening in Northern Hemisphere summer storm tracks from Eulerian metrics, such as eddy kinetic energy[67] and mean sea level pressure fields[68], and from Lagrangian-based extratropical cyclone properties, such as frequency[69] and wind speed[70].

The right column of Fig. 7 displays the JJA climatological Z500 eddy field from SPEAR simulations in both historical and SSP5-8.5 scenarios. As indicated by the differences between the two periods (Fig. 7D), the reduced intensity of climatological Z500 stationary eddies is pronounced over the North Pacific Ocean (e.g., 30°–50°N), consistent with previous findings[71]. This contrasts with the strengthened eddies over the southwestern U.S. where sharp increases in the probability of record-breaking daily maximum temperature are expected[7], as well as the relatively muted response over the Pacific Northwest. In line with the projected changes in North Pacific stationary eddies, we remind that the intensity of the upstream Rossby wave train traversing the North Pacific during WNA heatwave events tends to be weaker in the future period (Fig. 3). This collocation of weaker climatological stationary eddies and transient eddies is indicative of weaker interference between eddies over the North Pacific[37,72], which warrants further investigation.

Next, we examine the upper tropospheric temperature gradient response to climate change in SPEAR. This analysis is motivated by a recent study that examined the responses of atmospheric waves to climate change in terms of zonal wavenumber[73]. They found that the amplitudes of midlatitude synoptic-scale waves (i.e., wavenumbers equal to or greater than 6) are projected to decrease in all seasons, whereas those of large-scale waves strengthen. Based on the linear normal-mode instability analysis, they attributed these scale-dependent changes in the growth rate of waves to the effect of the mean upper tropospheric zonal wind, which is related to an increase in the meridional temperature gradient (i.e., enhanced tropical upper tropospheric warming). Figure 8A illustrates the JJA 250-hPa meridional temperature gradients (ΔT_{250}) measured by the regional temperature differences (i.e., 60°–80°N minus 20°–40°N)[74] in the two different periods. It is clearly shown that the magnitude of ΔT_{250} in SPEAR is projected to increase due to more rapid warming in the tropical upper troposphere[75], which is quantitatively confirmed by the boxplots (Fig. 8B). In the late twenty-first century period, the median linear trend of ΔT_{250} exhibits an increase of approximately 0.2 K per decade relative to that of the recent historical period, consistent with the previous finding. We note that all trends in both periods are statistically significant at the $p < 0.001$ level assessed by the non-parametric Mann–Kendall test[76].

In Fig. 8C–E, we further examine if appreciable changes in the meridional temperature gradient on the intraseasonal time scale are found during WNA heatwaves. The composites of detrended zonal-mean 250-hPa temperature anomalies show that the upper tropospheric temperature gradient prior to the onset of heatwave events generally increases in both periods. Although there are notable differences such as anomalous cooling at mid-to-high latitudes (e.g., north of 70°N, 30°–50°N band) and warming

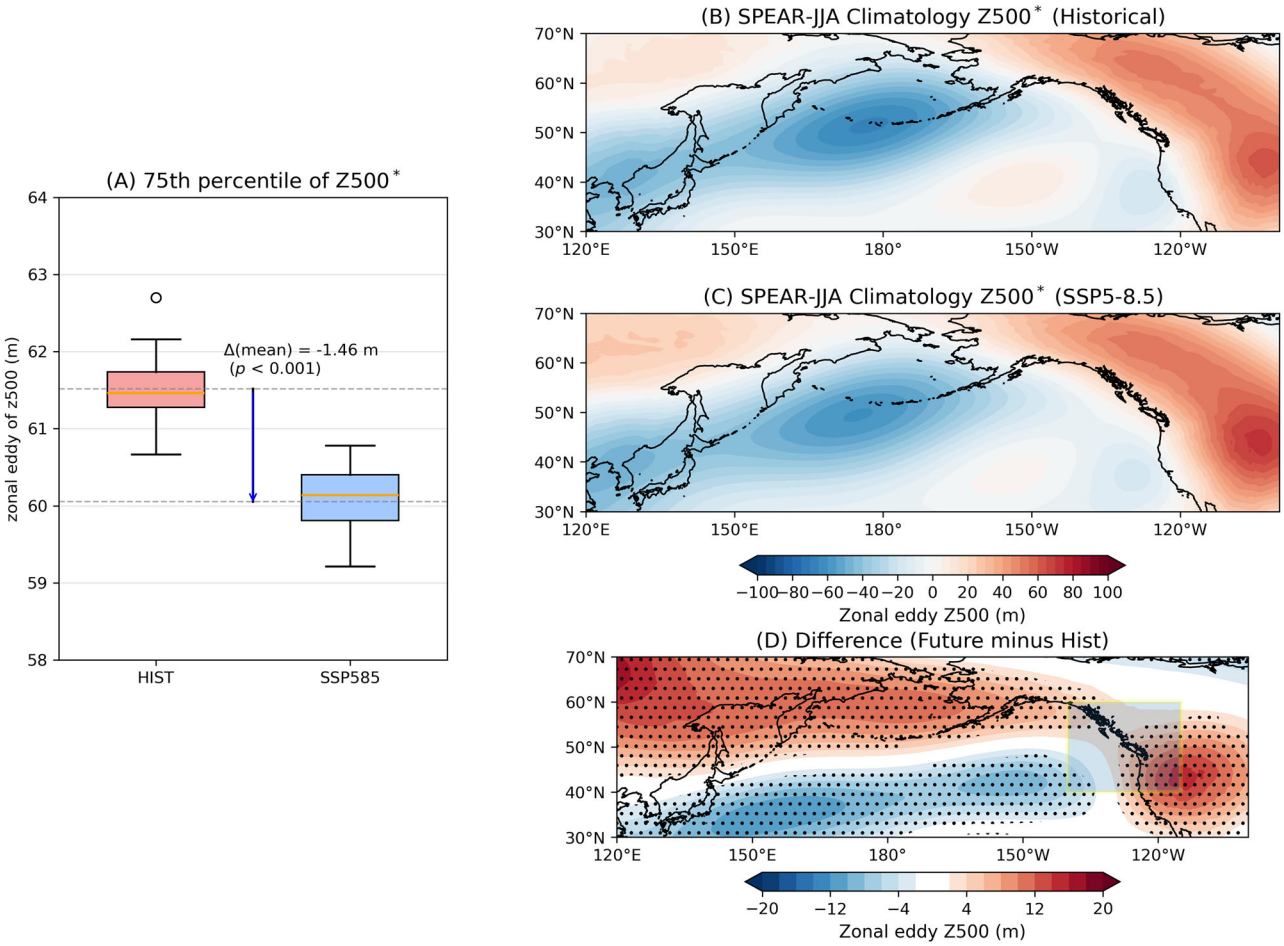

Fig. 7 | Projected changes in the boreal summer North Pacific Z500 eddy fields from SPEAR. A Boxplots of the 75th percentile of 500-hPa zonal geopotential height eddies (Z500*) in the Northern Hemisphere midlatitudes (40°–80°N) during the historical and late twenty-first century JJA periods. The medians of the model ensemble distribution are indicated by thin orange lines. **B**–**D** Spatial map of 250-hPa JJA climatological Z500* during the **B** recent historical period, **C** late twenty-first century period under SSP5-8.5, and **D** their differences. In **D**, only regions where at least 80% of ensemble members agree on the sign of the difference are shaded, and yellow box denotes the WNA domain used in this study. Stippling indicates statistical significance at the 5% level, evaluated using Welch's *t*-test.

at the 50°–70°N band (Fig. 8E), the change in the meridional gradient is small. Therefore, we conclude that intraseasonal change in the meridional temperature gradient does not play a crucial role in moderating the circulation intensity during WNA heatwaves.

Lastly, we turn our attention to projected changes in the Pacific jet stream from SPEAR simulations, which serves as a Rossby waveguide that constrains the propagation of the Rossby wave perturbation[77,78]. The climatological westerly jet streams at 250 hPa from the historical and future periods are shown in Fig. 9A–C. Consistent with the mid tropospheric circulation (e.g., Fig. 6) and storm track intensity responses to climate change[66], the overall Pacific jet intensity substantially weakens, particularly over the jet entrance region (Fig. 9C). As the synoptic-scale wave energy tends to propagate zonally within the narrow atmospheric jets according to stationary wave theory[77] and upper-level divergence occur at the poleward flank of the jet exit[79], the location of jet exit affects where meridional divergent outflow develops. In Fig. 9D, E, we show the tail of the Pacific jet by illustrating only wind speeds greater than 18 m s^{-1}. The 18 m s^{-1} isotach in the historical period nearly reaches the western boundary of the WNA domain used in this study. In the future projection, however, we clearly see the weakening and retreating of the jet structure within the 18 m s^{-1} isotach (Fig. 9F), suggesting that the probability of synoptic-scale waves propagation toward western North America is reduced and that the preferred location of meridional divergent outflow in the future may shift westward.

As a further step, we quantitatively investigate the properties of the boreal summer jet stream, namely its location and intensity. Here, we define these two metrics as the location and magnitude of the maximum 250-hPa zonal mean zonal wind, respectively, identified by a quadratic fit of local maximum and its two adjacent grid points[80]. The latitudinal profile of zonal mean zonal wind field in Fig. 9G again corroborates that the boreal summer jet is projected to weaken while maintaining its general structure, which is demonstrated by the boxplots of jet properties (Fig. 9H). The median of simulated jet intensity decreases by approximately 1.5 m s^{-1}, whereas the jet locations exhibit a minimal change. While the connection between jets and waves remains an active area of research, recent waveguide studies support the idea that weaker jets are likely to serve as weaker waveguides, leading to smaller midlatitude wave amplitudes[78]. In light of the above, we conclude that weaker midlatitude jets in a warming climate serve as a key contributor to weaker amplitudes of the synoptic-scale wave circulation during boreal summer.

Discussion

Western North America (WNA) regularly experiences daily extreme temperature anomalies associated with intense synoptic-scale circulation activity—as evidenced by the 2021 Pacific Northwest case, making the region a hotspot for heat extremes in the midlatitudes[13,20,34,81]. The present study leverages high-resolution large-ensemble simulations (i.e., a 50-km atmospheric horizontal resolution and a nominal 1.0° ocean horizontal resolution; see Methods) generated by GFDL SPEAR to obtain a sufficient number of WNA heat extreme cases and gain insights into the general properties of WNA heatwaves and the associated atmospheric processes.

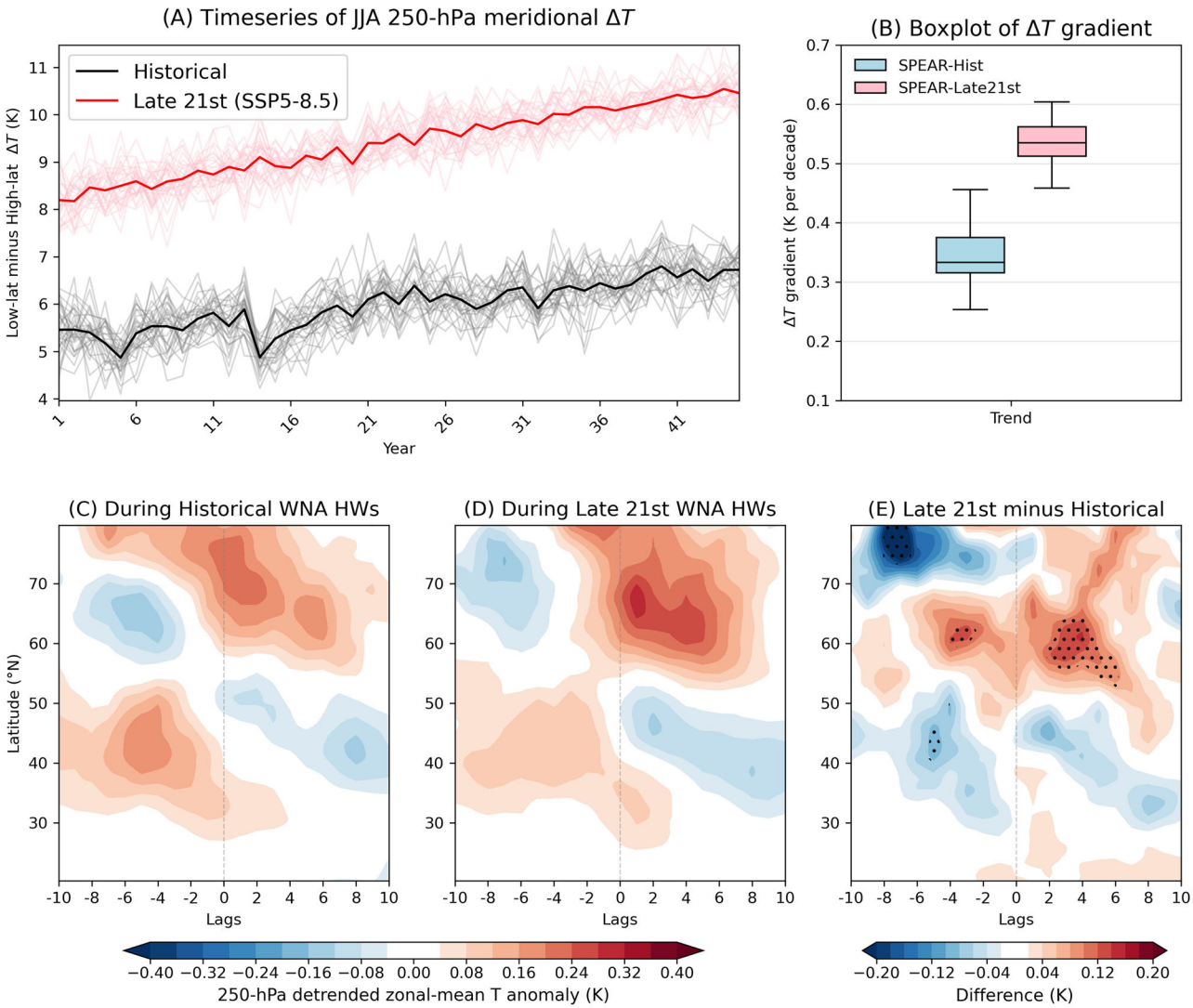

Fig. 8 | Projected changes in the boreal summer 250-hPa meridional temperature gradient from SPEAR. A Timeseries of JJA 250-hPa meridional temperature gradient (ΔT_{250}) measured by the difference in zonally averaged temperature between the high latitudes (60°–80°N) and low latitudes (20°–40°N). **B** Boxplots of the linear trends in ΔT_{250} (K per decade) in all SPEAR ensemble members during the recent historical period and late twenty-first century period under SSP5-8.5. The medians of the model ensemble distribution are indicated by thin black lines. Lag composites of detrended 250-hPa zonal-mean temperature anomalies during the **C** historical WNA heatwave events, **D** future WNA heatwave events, and **E** their differences. In **E**, stippling indicates statistical significance at the 5% level, evaluated using Welch's *t*-test.

After removing the effects of the seasonal cycle and long-term trends, we show that the geographical distribution of WNA heat extreme occurrences during the recent historical period (i.e., 1979–2023 JJA) is elevated relative to surrounding land regions (Fig. 1); however, this hotspot feature dissipates under future warming scenarios (Fig. 2).

The intraseasonal evolution of WNA heat extremes and associated atmospheric processes was examined to address the question of whether this projected reduction is driven by a diminished role of zonally asymmetric atmospheric process, particularly atmospheric blocking. In order to focus on daily synoptic-scale variations of these extreme events, we have employed a feature-tracking algorithm to identify heatwaves of varying shapes and morphologies that are centered over WNA. The lag composite analysis for the WNA heatwave events for each period reveals that the following chain of atmospheric processes is a common thread of WNA heatwaves in both periods: (1) A Rossby wave packet is generated over the western North Pacific and gradually propagates eastward. (2) Moisture flux anomalies propagating along this wave packet tend to create a narrow and intense poleward transport (sometimes detected as atmospheric river activity) at the western flank of anticyclonic circulation over WNA, leading to maintenance and amplification of the ridge. (3) This quasi-stationary and persistent ridge, often as blocking, contributes to the occurrence of WNA heatwaves, through physical processes that drive surface warming[11,26]. However, in a future emissions scenario, we find that the blocked area is of broader extent and accompanied by farther poleward moisture transport but weaker upstream wave train magnitudes during WNA heatwave events (Fig. 3).

We have performed a quantitative analysis on these projected changes in the properties of WNA heatwaves and their linkages to associated atmospheric physical processes with a heatwave-centered diagnostic approach. Our results show that in the future projection, moisture transport at the northern flank of heatwaves is considerably enhanced (i.e., by approximately 27% compared to the historical period) corresponding to increased atmospheric moisture availability[38] and atmospheric river activity[82] in a warming climate. We also find atmospheric blocking co-occurs with WNA heatwaves more frequently with a larger areal extent but slightly reduced peak intensity in the late twenty-first century period (Fig. 4). These structural changes in atmospheric moisture transport, blocking, and heatwaves are consistently shown in the WNA blocking-centered composites (Fig. 6), further demonstrating that projected changes in the properties of WNA heatwaves are closely linked to changes in atmospheric processes.

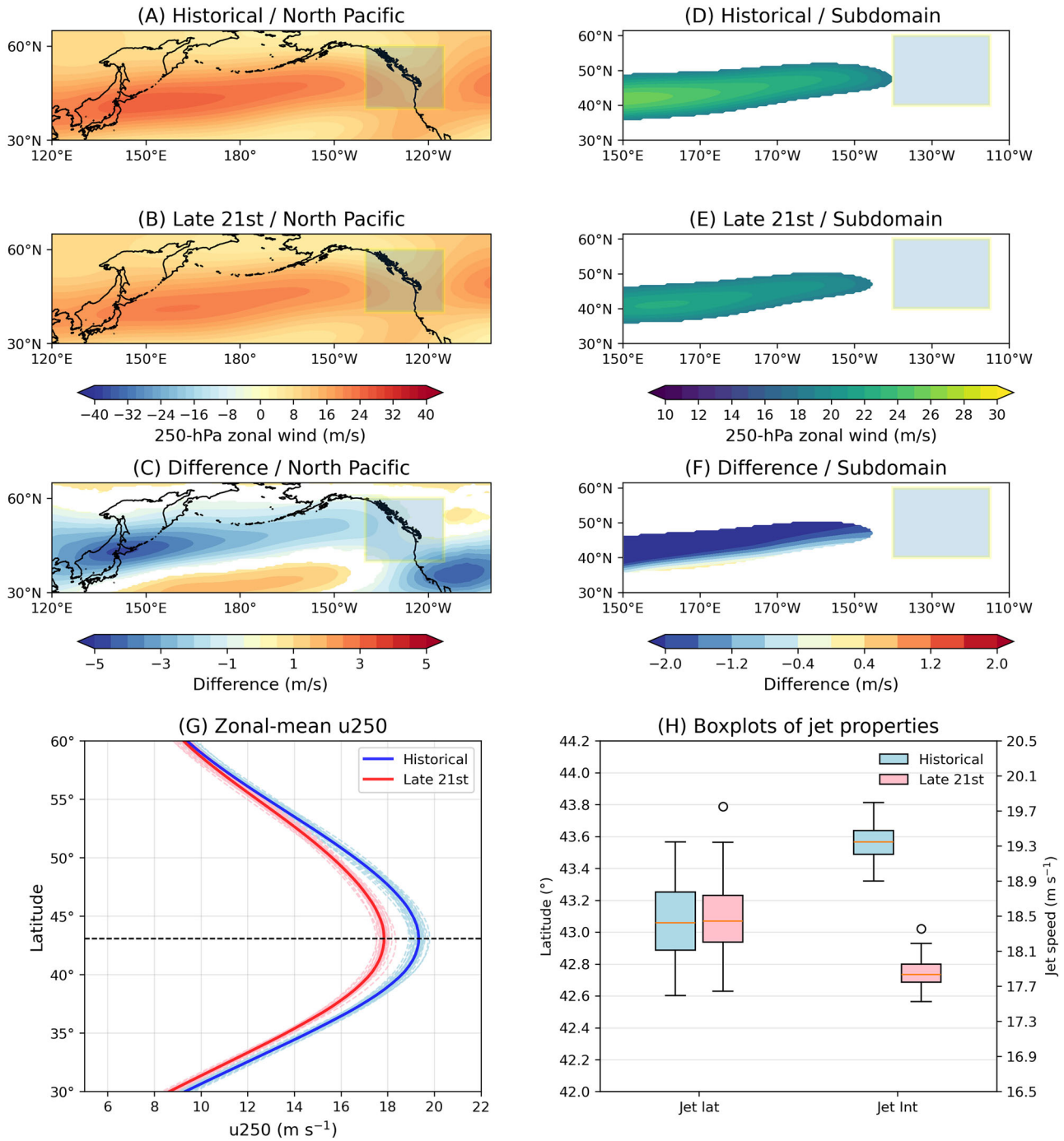

Fig. 9 | Projected changes in the boreal summer 250-hPa westerly jet stream from SPEAR. A–C Spatial map of 250-hPa JJA climatological zonal wind during the **C** recent historical period, **D** late twenty-first century period under SSP5-8.5, and **E** their differences. **D–F** As in **C–E** but with wind speed equal to or greater than 18 m s^{-1} over a subdomain (30°–60°N, 150°E–110°W). In **C**, **F**, only regions where at least 80% of ensemble members agree on the sign of the difference are shaded. Yellow boxes from **A–F** denote the WNA domain used in this study. **G** Latitudinal profile of 250-hPa JJA climatological zonal mean zonal wind from the recent historical period (blue) and late twenty-first century period (red) for the ensemble mean (solid line) and individual members (dashed lines). Horizontal lines indicate the mean location of the climatological jet from SPEAR ensemble members for both periods (black dashed line). **H** Boxplots of climatological jet location and intensity during the two periods. The medians of the model ensemble distribution are indicated by thin orange lines, while white circles represent outliers.

Our results on the projected changes in the background mean state of atmospheric circulation suggest that overall weaker synoptic-scale circulation anomalies during WNA heatwave events are associated with projected weakening in the climatological stationary eddies (Fig. 7), enhanced upper tropospheric tropical warming (Fig. 8), and jet intensity over the North Pacific (Fig. 9). We particularly emphasize the substantial weakening of the upper tropospheric jet stream intensity with minimal changes in jet location, as the simulated co-occurrence of reduced WNA heatwave frequency and weaker Pacific jets is consistent with the recent studies linking the projected reduction in midlatitude synoptic-scale wave amplitudes to weaker jets serving as waveguides[78]. A more detailed analysis of Rossby waveguides and their impacts on WNA heatwaves are left for a future work.

Another priority for future research is to understand and diagnose why models systematically underrepresent longitudinal variation in WNA

heatwaves relative to observations (e.g., Fig. 1D–F). Considering the importance of upstream synoptic-scale circulation for regional temperature variability, we show the 250-hPa JJA climatological synoptic-scale eddy kinetic energy (EKE) from SPEAR and ERA5 in Fig. S7. The synoptic-scale EKE in ERA5 is almost evenly distributed across the North Pacific, whereas the SPEAR-MED ensemble mean exhibits synoptic-scale eddy disturbances concentrated over the western North Pacific that does not extend sufficiently into the eastern North Pacific. A similar underestimation over WNA is found in the climatological zonal wind speed, in spite of the model's reasonable performance in capturing zonal mean jet properties (Fig. S8). This weaker mean upper-level circulation in SPEAR may reflect an overall underestimation of synoptic-scale eddy activity toward WNA and a diminished role of atmospheric jets as Rossby waveguides[78], thus acting as a possible source of bias. It is also noteworthy that climate models generally struggle to simulate the summertime extratropical cyclone track density over the eastern North Pacific Ocean[83], implying that synoptic-scale eddies affecting WNA during boreal summer tend to be underrepresented from both Eulerian and Lagrangian perspectives, which warrants further investigation.

Other possible causes behind these biases in SPEAR are listed as follows: (1) Model bias in land-atmosphere interaction. Although the land model of the SPEAR modeling system, LM4, has incorporated dynamic vegetation and improved the representation of land surface properties relative to previous generations of GFDL models[84], biases in soil moisture and evapotranspiration persist, partly due to limited representation of land-atmosphere interaction[85]. (2) Model bias in tropical-extratropical interaction. Recent studies have shown that extratropical teleconnections triggered by tropical convective activity, particularly those associated with the Boreal Summer Indian Oscillation (BSISO), can enhance the likelihood of heat extreme occurrences over the Pacific Northwest[86]. We conjecture that errors in simulating this tropical-extratropical interaction in SPEAR, including errors in simulating BSISO[87] and its teleconnections, may contribute to the bias in the simulated WNA heatwave occurrences. (3) Coarser ocean horizontal resolution and topographic variations in this version of SPEAR (SPEAR-MED): The SPEAR-MED simulations used in this study adopt a relatively coarse ocean horizontal resolution for computational efficiency (i.e., 1° with tropical refinement to 0.3°)[84] and simplified topography, compared with other versions currently under development. This practical decision may introduce biases in surface turbulent fluxes resulting from the inability to resolve oceanic mesoscale eddies, as well as underestimated adiabatic warming resulting from the model's flattened topography, both of which in turn influence downstream atmospheric circulation variability. Future modeling efforts to reduce these possible biases will help improve the representation of regional heat extreme occurrences, including hotspots such as WNA.

The overall reduction in WNA heatwave occurrences in the SPEAR large ensemble (i.e., approximately 11%, Fig. S4) reflects decreased T_{max} skewness in the projections (e.g., Fig. S2), after accounting for the effect of mean temperature increases. This is generally consistent with the projected decline in boreal summer mid- to high-latitude blocking frequency[35,71,88] and storm track activity[67,70], suggesting a reduced likelihood of synoptic-scale circulation anomalies contributing to the development of intense heat extremes over WNA throughout the analyzed period. However, this does not necessarily imply that the influence of atmospheric processes on regional temperature extremes will weaken under future emissions scenarios, since a broader moisture transport and atmospheric blocking area may also broaden the impacts and lead to more expansive region of anomalous heat. Even a small increase of temperature anomaly, once combined with increasing mean temperature trends under future emissions scenario, can result in an unprecedented extreme temperature event[6] and exacerbate adverse impacts of regional heatwaves[45]. In this regard, the need for accurate prediction and projection of heatwaves will likely remain high in the future, both to minimize adverse impacts of heatwaves on human health and ecosystems[8,11,15,89] and to support the timely development of adaptation and mitigation strategies[26].

The present study shows that a distinct Rossby wave pattern is captured by SPEAR approximately 1–2 weeks prior to the development of WNA heatwaves, a feature that is often recognized as a potential source of predictability for extreme weather events over North America[28,37,86,90,91]. The model representation of upstream wave train affects the capability of capturing moist process and their feedback on downstream blocking[55]. In the case of the 2021 Pacific Northwest heatwave, for instance, previous studies found that operational subseasonal-to-seasonal forecast models were able to reasonably predict the location of the heatwave and associated blocking up to 10–20 days in advance, capturing a similar Rossby wave train across the North Pacific as seen in the composite analysis of this study[15,24]. However, models struggle to reproduce the intensity of this heatwave, possibly due to their failure to capture the upstream moisture transport driven by AR activity along the wave train[23,24]. Our results suggest that this upstream wave packet, accompanied by anomalous moisture transport, is a key process in the development not only of the 2021 Pacific Northwest case, but of WNA heatwaves more generally. In light of recent findings that tropical variability, such as the Boreal Summer Indian Oscillation[86] and Southeast Asian monsoon[24,25], can excite a Rossby wave train propagating toward North America, further investigation into the driving mechanisms of the wave train during WNA heatwaves is currently underway.

Amid the ongoing warming trend, marked by a record breaking 1.5 °C increase in global mean temperature above pre-industrial level[1], a continued rise in the frequency of global temperature extremes appears inevitable. However, the regional characteristics of projected heatwaves are more complex than simple monotonic increases, as demonstrated by our findings on projected changes in WNA heatwaves and their linkages to atmospheric processes. The escalating likelihood of record-breaking temperature extremes in a warming climate[6,7] underscores the need for further region-specific studies to provide information tailored to communities and stakeholders for effective adaptation and societal preparedness.

Methods

Data

In this study, we use a 30-member large ensemble of simulations from a fully coupled model, the Seamless System for Prediction and Earth System Research (SPEAR). The SPEAR model, developed by the National Oceanic and Atmospheric Administration (NOAA) Geophysical Fluid Dynamics Laboratory (GFDL), is one of the latest modeling systems designed to improve scientific understanding of Earth system variability, predictability, and projected changes across a wide range of time scales. The model employs the state-of-the-art component models from GFDL, including the AM4 atmosphere model, LM4 land model, SIS2 sea ice model, and MOM6 ocean model, with moderately adjusted configurations optimized for simulating long-term variability of the Earth system under different scenarios. Each ensemble member is initialized by different initial conditions derived from a long-term control simulation with a 20-year interval. We refer readers to ref. 84 for further details. While SPEAR offers several options for horizontal resolution configurations, with a common 33-vertical level and 1.0° × 1.0° ocean grid refined to 0.3° in the tropics[92], a 50-km atmospheric horizontal resolution (i.e., SPEAR-MED) version has been utilized in this study. The relevance of SPEAR-MED for an investigation of regional heat extreme over North America has been demonstrated by recent studies[7,33,34].

To examine how characteristics of heatwaves over western North America and related atmospheric processes change in a warming climate, we analyze two different 45-year periods—the recent historical (1979–2023) boreal summers (June-July-August, JJA) and the late twenty-first century (2056–2100) boreal summers. All SPEAR simulations follow the Coupled Model Intercomparison Project Phase 6 (CMIP6)[40] protocol for radiative forcing; the model simulations are forced by CMIP6 historical forcing until 2014 and then forced by radiative forcing under different emissions scenarios, specifically the Shared Socioeconomic Pathway 5-8.5 (SSP5-8.5) and SSP2-4.5 scenarios. For the recent historical period, as in ref. 37, we use the first 36 boreal summers from the historical simulations and the remaining

summers from the SSP5-8.5 simulations. Note that global and regional temperature differences across future emissions scenarios are marginal for the first 10 years of future projections[7,14] (i.e., 2015–2024). Throughout this study, unless noted otherwise, daily anomalies are computed by removing the seasonal cycle, smoothed by retaining the first 10 harmonics of the calendar-day-mean values.

For observational reference, we use the global daily maximum near-surface air temperature (T_{max}) data from the NOAA Climate Prediction Center (CPC)[93], which has a 0.5° × 0.5° horizontal resolution, to validate the simulated regional hot spot of heat extremes over North America (Fig. 1). This data has been regridded to the native resolution of SPEAR-MED for a fair comparison. Moreover, to compare SPEAR's performance in simulating heat extremes with that of other climate models, we also analyze corresponding simulations from 29 CMIP6 models, based on the availability of daily T_{max} data (Table S1).

Identification of heat extremes and heatwave events

An impact driven by intraseasonal atmospheric circulation on regional temperature variation can be accurately assessed when the effects of the long-term trend and seasonal cycle are removed[41]. To this end, we defined heat extremes as described in the ref. 57, in which the seasonal cycle and long-term trends are removed from daily maximum near-surface air temperature data while accounting for their non-stationarity. Specifically, we first applied a 5-day moving average to daily maximum temperature to filter out high-frequency weather noise. Next, to remove the seasonal cycle and interdecadal trend, we subtracted centered 29-calendar day × 11-year moving averages, allowing a slowly varying seasonal cycle to reflect its non-stationarity. The resultant variable is termed as the T_{max} anomaly. This anomaly is calculated separately for the two analysis periods by removing the corresponding seasonal cycle and long-term trends. Lastly, we identified all JJA 5-day periods when the grid point T_{max} anomaly exceeds its 2.0 local standard deviation (i.e., approximately the top 2.5% of warmest 5-day periods under a Gaussian distribution). The results of this study are qualitatively consistent, though fewer cases are identified when using the 2.3 standard deviation threshold, as in the ref. 57. This anomaly-based definition is adopted in this study to explore the linkage between heat extreme frequency over North America and synoptic-scale atmospheric variability, such as atmospheric blocking. Meanwhile, we note that the results are not qualitatively sensitive to the specific definition of T_{max} anomaly (e.g., using a stationary seasonal cycle, as described in the "Data" section).

Considering that synoptic-scale atmospheric circulation affects surface temperature on a similar spatial scale[28,35,48], we propose a novel methodology to identify a synoptic-scale heatwave event over western North America. First, 5-day heat extremes were identified following the method described above, but only at grid points with at least 80% land coverage[7] (e.g., Fig. 1). Next, we applied an object-tracking algorithm (i.e., the ConTrack-Contour Tracking)[52] that considers the connectivity of nearby grid points that also meet the criteria for a heat extreme to isolate T_{max} anomaly "blobs" over land. We then calculate the area of the T_{max} anomaly blobs and define those that exceed an area threshold of 10^6 Km^2 as a synoptic-scale heatwave[81]. For each identified temperature blob, we compute a center of mass (i.e., the mean location of T_{max} anomaly distribution in the blob). If this center of mass is located within the WNA domain (i.e., 40°–60°N, 140°–115°W; green boxes in Fig. 1), this day is defined as a WNA heatwave event. As an example of event identification, Fig. S3 shows the 5-day average T_{max} anomaly field simulated by the first ensemble member centered on 2008-08-02 in the upper left panel, the identified T_{max} anomaly blob in the upper right panel, and its center of mass in the lower right panel, marked by a yellow star. Leveraging the advantage of a large ensemble dataset, heatwave event detection was performed for all 30 ensemble members, which results in total 1610 WNA events during the recent historical period and 1450 events during the late twenty-first century period (Fig. S4). Among the detected heatwave event days, consecutive WNA heatwave events are frequently found, reflecting the long duration of many events. For the composite analysis in Fig. 3, we define the onset day of a heatwave as the first central day (within the 5-day window) that the WNA heatwave event criteria are reached. These onset days are separated by at least 7 days, sufficiently exceeding the *e*-folding timescale of the T_{max} autocorrelation in WNA (i.e., approximately 3 days).

For the evaluation of the general heatwave-blocking relationship shown in Fig. S6, following ref. 45, we use the warm spell duration index[61] that defines heatwaves as days when daily T_{max} anomalies (i.e., without a 5-day moving average) exceed the local 90th percentile for at least 6 consecutive days.

Atmospheric river identification

An atmospheric river (AR) is an intense and narrow plume of moisture transport effected by a synoptic-scale weather system, often associated with torrential moisture transport and related extreme precipitation[94,95]. Atmospheric river activity has been further linked to regional temperature extremes[60], as suggested for the 2021 Pacific Northwest heatwave event[23,24]. Previous studies using SPEAR-MED have shown that the model reproduces the key observed characteristics of atmospheric river climatology across seasons[95] and is suitable for investigating AR projections and predictions[36,96]. Following these prior studies, we track ARs by using a detection algorithm introduced by ref. 97 for the analysis periods. This detection algorithm tests whether the integrated vapor transport (IVT) anomaly at a given grid point meets specified intensity and geometry criteria, capturing the filamentary structure of ARs. In this study, given the available SPEAR-MED outputs, IVT is computed as follows:

$$\mathrm{IVT} = \frac{1}{g}\sqrt{\left(\int_{1000}^{250} uq\,dp\right)^2 + \left(\int_{1000}^{250} vq\,dp\right)^2}$$

where u, v correspond to the zonal and meridional wind, respectively, and q corresponds to the specific humidity, and g is the gravitational acceleration. Prior to an AR detection, an IVT anomaly is computed by removing the seasonal cycle smoothed by retaining the first 10 harmonics of the calendar-day mean values. An AR is detected if a contiguous IVT anomaly exceeds 125 $kg\,m^{-1}s^{-1}$, spans at least 150 grid points, and exhibits an aspect ratio of at least 1.4, serving as the intensity, area, and geometry threshold, respectively[36,95–97]. While the fixed thresholds are implemented to examine projected changes in AR frequency associated with WNA heatwaves, these results are likely to be influenced by the choice of the thresholds. For instance, using the time-varying thresholds for AR detection in SPEAR-MED simulations, a previous study found that the estimated AR time of emergence is delayed by approximately two decades over most regions[36]. Therefore, caution is warranted when interpreting projected increases in upstream AR frequency during WNA heatwave events, as such increases may be reduced if a stronger IVT magnitude threshold is used for AR detection.

Atmospheric blocking identification

Atmospheric blocking refers to a quasi-stationary and persistent anticyclonic circulation pattern that has been extensively studied for its connection to surface temperature extremes, both locally and remotely[54,88]. To identify local blocking associated with WNA heatwaves, this study employs an anomaly-based blocking index, among different metrics of atmospheric blocking, that tests whether local 500-hPa geopotential height (Z500) anomalies meet thresholds for intensity, area, consecutiveness, and persistence[29,45,98]. This choice is based on previous findings that omega-shaped blocking preferentially develops over western North America during boreal summer[99], which is well captured by the anomaly-based detection method[29,100]. Specifically, we first compute the daily Z500 anomaly amplitude threshold for blocking, defined as 1.3 standard deviations of Z500 anomalies over 30°–80°N within a 3-month window centered on the target month. The Z500 anomaly that meets or exceeds the amplitude threshold is considered as a blocking candidate. These blocking candidates then must

pass the area threshold ($\geq 2.0 \times 10^6$ km^2), have at least 50% spatial overlap within consecutive days, and persist for a minimum of 5 days to be defined as a blocking event. This detection procedure was carried out using the previously introduced Python package ConTrack-Contour Tracking[52]. The blocking index is calculated separately for each ensemble member and analysis period. Previous blocking studies using GFDL models have shown that these models generally perform well in capturing regional blocking characteristics and variability across different generations and configurations[65], including SPEAR[98]. However, they tend to moderately underestimate zonal eddies in Z500 during boreal summer over the Northern Hemisphere midlatitudes[65]. This weaker amplitude of geopotential height eddy intensity may have partly contributed to a negative bias in the zonal asymmetry of WNA heat extremes (Fig. 1).

Data availability

All data used in this study are publicly available. NOAA-CPC global daily maximum/minimum temperature and precipitation data can be downloaded from https://psl.noaa.gov/data/gridded/index.html. SPEAR Large ensemble data can be downloaded from https://www.gfdl.noaa.gov/spear_large_ensembles/. The CMIP6 model output used in this study is available at https://aims2.llnl.gov/search/cmip6/. The ERA5 reanalysis hourly data used in the Supplementary Information can be downloaded from https://cds.climate.copernicus.eu/datasets/reanalysis-era5-pressure-levels?tab=overview for pressure levels.

Code availability

The feature tracking algorithm code used in this study is a Python open-source package, CONTRACK, which is accessible from https://github.com/steidani/ConTrack[52]. Other custom scripts directly implement the statistical methods and techniques described in the "Methods" section.

Received: 18 June 2025; Accepted: 31 December 2025;
Published online: 13 January 2026

References

1. World Meteorological Organization. *State of the Global Climate 2024* (World Meteorological Organization, 2025).
2. Meehl, G. A. & Tebaldi, C. More intense, more frequent, and longer lasting heat waves in the 21st century. *Science* **305**, 994–997 (2004).
3. Donat, M. G., L. V. Alexander, N. Herold, & A. J. Dittus. Temperature and precipitation extremes in century-long gridded observations, reanalyses, and atmospheric model simulations. *J. Geophys. Res. Atmos.* **121**, 11,174–11,189 (2016).
4. Seneviratne, S. I. et al. in *Climate Change 2021: The Physical Science Basis. Contribution of Working Group I to the Sixth Assessment Report of the Intergovernmental Panel on Climate Change* (eds Masson-Delmotte, V. et al.) 1513–1766 (Cambridge University Press, 2021).
5. Rahmstorf, S. & Coumou, D. Increase of extreme events in a warming world. *Proc. Natl. Acad. Sci. USA* **108**, 17905–17909 (2011).
6. Fischer, E. M., Sippel, S. & Knutti, R. Increasing probability of record-shattering climate extremes. *Nat. Clim. Chang.* **11**, 689–695 (2021).
7. McHugh, C. E., Delworth, T. L., Cooke, W. & Jia, L. Using large ensembles to examine historical and projected changes in record-breaking summertime temperatures over the Contiguous United States. *Earths Future* **11** https://doi.org/10.1029/2023ef003954 (2023).
8. Matthews, T. et al. Humid heat exceeds human tolerance limits and causes mass mortality. *Nat. Clim. Change* **15**, 4–6 (2024).
9. Ting, M. et al. Contrasting impacts of dry versus humid heat on US corn and soybean yields. *Sci. Rep.* **13**, 710 (2023).
10. Richardson, D. et al. Global increase in wildfire potential from compound fire weather and drought. *npj Clim. Atmos. Sci.* **5**, 23 (2022).
11. Tian, Y. et al. Characterizing heatwaves based on land surface energy budget. *Commun. Earth Environ.* **5** https://doi.org/10.1038/s43247-024-01784-y (2024).
12. Barriopedro, D., Fischer, E. M., Luterbacher, J., Trigo, R. M. & García-Herrera, R. The hot summer of 2010: redrawing the temperature record map of Europe. *Science* **332**, 220–224 (2011).
13. McKinnon, K. A., Rhines, A., Tingley, M. P. & Huybers, P. The changing shape of Northern Hemisphere summer temperature distributions. *J. Geophys. Res. Atmos.* **121**, 8849–8868 (2016).
14. Seneviratne, S. I., Donat, M. G., Pitman, A. J., Knutti, R. & Wilby, R. L. Allowable CO2 emissions based on regional and impact-related climate targets. *Nature* **529**, 477–483 (2016).
15. White, R. H. et al. The unprecedented Pacific Northwest heatwave of June 2021. *Nat. Commun.* **14**, 727 (2023).
16. Thompson, V. et al. The 2021 western North America heat wave among the most extreme events ever recorded globally. *Sci. Adv.* **8**, eabm6860 (2022).
17. Zhang, Y. & Boos, W. R. An upper bound for extreme temperatures over midlatitude land. *Proc. Natl. Acad. Sci. USA* **120**, e2215278120 (2023).
18. Schumacher, D. L., Hauser, M. & Seneviratne, S. I. Drivers and mechanisms of the 2021 Pacific Northwest heatwave. *Earths Future* **10** https://doi.org/10.1029/2022ef002967 (2022).
19. Neal, E., Huang, C. S. Y. & Nakamura, N. The 2021 Pacific Northwest heat wave and associated blocking: meteorology and the role of an upstream cyclone as a diabatic source of wave activity. *Geophys. Res. Lett.* **49** https://doi.org/10.1029/2021gl097699 (2022).
20. Yu, B., Lin, H., Mo, R. & Li, G. A physical analysis of summertime North American heatwaves. *Clim. Dyn.* **61**, 1551–1565 (2023).
21. Röthlisberger, M. & Papritz, L. Quantifying the physical processes leading to atmospheric hot extremes at a global scale. *Nat. Geosci.* **16**, 210–216 (2023).
22. Li, X. et al. Role of atmospheric resonance and land-atmosphere feedbacks as a precursor to the June 2021 Pacific Northwest Heat Dome event. *Proc. Natl. Acad. Sci. USA* **121**, e2315330121 (2024).
23. Mo, R., Lin, H. & Vitart, F. An anomalous warm-season trans-Pacific atmospheric river linked to the 2021 western North America heatwave. *Commun. Earth Environ.* **3** https://doi.org/10.1038/s43247-022-00459-w (2022).
24. Lin, H., Mo, R. & Vitart, F. The 2021 Western North American heatwave and its subseasonal predictions. *Geophys. Res. Lett.* **49** https://doi.org/10.1029/2021gl097036 (2022).
25. Qian, Y. et al. Effects of subseasonal variation in the East Asian monsoon system on the summertime heat wave in Western North America in 2021. *Geophys. Res. Lett.* **49** https://doi.org/10.1029/2021gl097659 (2022).
26. Domeisen, D. I. V. et al. Prediction and projection of heatwaves. *Nat. Rev. Earth Environ.* **4**, 36–50 (2022).
27. Barriopedro, D., García-Herrera, R., Ordóñez, C., Miralles, D. G. & Salcedo-Sanz, S. Heat waves: physical understanding and scientific challenges. *Rev. Geophys.* **61** https://doi.org/10.1029/2022rg000780 (2023).
28. Loikith, P. C., Lintner, B. R. & Sweeney, A. Characterizing large-scale meteorological patterns and associated temperature and precipitation extremes over the Northwestern United States using self-organizing maps. *J. Clim.* **30**, 2829–2847 (2017).
29. Steinfeld, D. & Pfahl, S. The role of latent heating in atmospheric blocking dynamics: a global climatology. *Clim. Dyn.* **53**, 6159–6180 (2019).
30. Lee, H.-I. & Nakamura, N. Imprint of diabatic processes in the waviness of the jet stream: an analysis of local wave activity budget. *J. Clim.* **37**, 5703–5719 (2024).
31. Brunner, L., Schaller, N., Anstey, J., Sillmann, J. & Steiner, A. K. Dependence of present and future European temperature extremes

on the location of atmospheric blocking. *Geophys. Res. Lett.* **45**, 6311–6320 (2018).
32. Wehner, M. et al. Changes in extremely hot days under stabilized 1.5 and 2.0 °C global warming scenarios as simulated by the HAPPI multi-model ensemble. *Earth Syst. Dyn.* **9**, 299–311 (2018).
33. Jia, L. et al. Skillful seasonal prediction of North American summertime heat extremes. *J. Clim.* **35**, 4331–4345 (2022).
34. Labe, Z. M., Johnson, N. C. & Delworth, T. L. Changes in United States summer temperatures revealed by explainable neural networks. *Earths Future* **12** https://doi.org/10.1029/2023ef003981 (2024).
35. Nabizadeh, E., Lubis, S. W. & Hassanzadeh, P. The 3D structure of Northern Hemisphere blocking events: climatology, role of moisture, and response to climate change. *J. Clim.* **34**, 9837–9860 (2021).
36. Tseng, K. C. et al. When will humanity notice its influence on atmospheric rivers? *J. Geophys. Res. Atmos.* **127** https://doi.org/10.1029/2021jd036044 (2022).
37. Park, M., Johnson, N. C. & Delworth, T. L. The driving of North American climate extremes by North Pacific stationary-transient wave interference. *Nat. Commun.* **15**, 7318 (2024).
38. Held, I. M. & Soden, B. J. Robust responses of the hydrological cycle to global warming. *J. Clim.* **19**, 5686–5699 (2006).
39. Pfahl, S., O'Gorman, P. A. & Fischer, E. M. Understanding the regional pattern of projected future changes in extreme precipitation. *Nat. Clim. Change* **7**, 423–427 (2017).
40. Eyring, V. et al. Overview of the Coupled Model Intercomparison Project Phase 6 (CMIP6) experimental design and organization. *Geosci. Model Dev.* **9**, 1937–1958 (2016).
41. Di Luca, A., de Elía, R., Bador, M. & Argüeso, D. Contribution of mean climate to hot temperature extremes for present and future climates. *Weather Clim. Extrem.* **28**, 100255 (2020).
42. Marin, M., Feng, M., Phillips, H. E. & Bindoff, N. L. A global, multiproduct analysis of coastal marine heatwaves: distribution, characteristics, and long-term trends. *J. Geophys. Res. Oceans* **126** https://doi.org/10.1029/2020jc016708 (2021).
43. Duan, S. Q., Findell, K. L. & Wright, J. S. Three regimes of temperature distribution change over dry land, moist land, and oceanic surfaces. *Geophys. Res. Lett.* **47** https://doi.org/10.1029/2020gl090997 (2020).
44. Srivastava, A. K., Wehner, M., Bonfils, C., Ullrich, P. A. & Risser, M. Local hydroclimate drives differential warming rates between regular summer days and extreme hot days in the Northern Hemisphere. *Weather Clim. Extrem.* **45**, 100709 (2024).
45. Chan, P. W., Catto, J. L. & Collins, M. Heatwave–blocking relation change likely dominates over decrease in blocking frequency under global warming. *npj Clim. Atmos. Sci.* **5**, 68 (2022).
46. Shepherd, T. G. Atmospheric circulation as a source of uncertainty in climate change projections. *Nat. Geosci.* **7**, 703–708 (2014).
47. Tamarin-Brodsky, T., Hodges, K., Hoskins, B. J. & Shepherd, T. G. Changes in Northern Hemisphere temperature variability shaped by regional warming patterns. *Nat. Geosci.* **13**, 414–421 (2020).
48. Loikith, P. C. & Broccoli, A. J. Characteristics of observed atmospheric circulation patterns associated with temperature extremes over North America. *J. Clim.* **25**, 7266–7281 (2012).
49. Byrne, M. P. & O'Gorman, P. A. Trends in continental temperature and humidity directly linked to ocean warming. *Proc. Natl. Acad. Sci. USA* **115**, 4863–4868 (2018).
50. Miralles, D. G., Teuling, A. J., van Heerwaarden, C. C. & Vilà-Guerau de Arellano, J. Mega-heatwave temperatures due to combined soil desiccation and atmospheric heat accumulation. *Nat. Geosci.* **7**, 345–349 (2014).
51. Prodhomme, C. et al. Seasonal prediction of European summer heatwaves. *Clim. Dyn.* **58**, 2149–2166 (2021).
52. Steinfeld, D., ConTrack - Contour Tracking. GitHub, https://github.com/steidani/ConTrack (2020).
53. Maddison, J. W., Gray, S. L., Martínez-Alvarado, O. & Williams, K. D. Impact of model upgrades on diabatic processes in extratropical cyclones and downstream forecast evolution. *Q. J. R. Meteorol. Soc.* **146**, 1322–1350 (2020).
54. Kautz, L.-A. et al. Atmospheric blocking and weather extremes over the Euro-Atlantic sector—a review. *Weather Clim. Dyn.* **3**, 305–336 (2022).
55. Wandel, J., Büeler, D., Knippertz, P., Quinting, J. F. & Grams, C. M. Why moist dynamic processes matter for the sub-seasonal prediction of atmospheric blocking over Europe. *J. Geophys. Res. Atmos.* **129** https://doi.org/10.1029/2023jd039791 (2024).
56. Hauser, S., Teubler, F., Riemer, M., Knippertz, P. & Grams, C. M. Life cycle dynamics of Greenland blocking from a potential vorticity perspective. *Weather Clim. Dyn.* **5**, 633–658 (2024).
57. Chan, P. W., Hassanzadeh, P. & Kuang, Z. Evaluating indices of blocking anticyclones in terms of their linear relations with surface hot extremes. *Geophys. Res. Lett.* **46**, 4904–4912 (2019).
58. Loikith, P. C., Singh, D. & Taylor, G. P. Projected changes in atmospheric ridges over the Pacific–North American region using CMIP6 models. *J. Clim.* **35**, 5151–5171 (2022).
59. Steinfeld, D., Sprenger, M., Beyerle, U. & Pfahl, S. Response of moist and dry processes in atmospheric blocking to climate change. *Environ. Res. Lett.* **17**, 084020 (2022).
60. Scholz, S. R. & Lora, J. M. Atmospheric rivers cause warm winters and extreme heat events. *Nature* **636**, 640–646 (2024).
61. Alexander, L. V. et al. Global observed changes in daily climate extremes of temperature and precipitation. *J. Geophys. Res. Atmos.* **111** https://doi.org/10.1029/2005jd006290 (2006).
62. Seneviratne, S. I. et al. Investigating soil moisture–climate interactions in a changing climate: a review. *Earth Sci. Rev.* **99**, 125–161 (2010).
63. Hsu, H. & Dirmeyer, P. A. Soil moisture-evaporation coupling shifts into new gears under increasing CO(2). *Nat. Commun.* **14**, 1162 (2023).
64. Fischer, E. M., Seneviratne, S. I., Vidale, P. L., Lüthi, D. & Schär, C. Soil moisture–atmosphere interactions during the 2003 European summer heat wave. *J. Clim.* **20**, 5081–5099 (2007).
65. Liu, P., Reed, K. A., Garner, S. T., Zhao, M. & Zhu, Y. Blocking simulations in GFDL GCMs for CMIP5 and CMIP6. *J. Clim.* **35**, 5053–5070 (2022).
66. Coumou, D., Di Capua, G., Vavrus, S., Wang, L. & Wang, S. The influence of Arctic amplification on mid-latitude summer circulation. *Nat. Commun.* **9**, 2959 (2018).
67. Lehmann, J., Coumou, D., Frieler, K., Eliseev, A. V. & Levermann, A. Future changes in extratropical storm tracks and baroclinicity under climate change. *Environ. Res. Lett.* **9**, 084002 (2014).
68. Harvey, B. J., Shaffrey, L. C. & Woollings, T. J. Equator-to-pole temperature differences and the extra-tropical storm track responses of the CMIP5 climate models. *Clim. Dyn.* **43**, 1171–1182 (2014).
69. Chang, E. K. M., Ma, C. G., Zheng, C. & Yau, A. M. W. Observed and projected decrease in Northern Hemisphere extratropical cyclone activity in summer and its impacts on maximum temperature. *Geophys. Res. Lett.* **43**, 2200–2208 (2016).
70. Priestley, M. D. K. & Catto, J. L. Future changes in the extratropical storm tracks and cyclone intensity, wind speed, and structure. *Weather Clim. Dyn.* **3**, 337–360 (2022).
71. Lackmann, G. M., Miller, R. L., Robinson, W. A. & Michaelis, A. C. Persistent anomaly changes in high-resolution climate simulations. *J. Clim.* **34**, 5425–5442 (2021).
72. Goss, M., Feldstein, S. B. & Lee, S. Stationary wave interference and its relation to tropical convection and Arctic warming. *J. Clim.* **29**, 1369–1389 (2016).

73. Chemke, R. & Ming, Y. Large atmospheric waves will get stronger, while small waves will get weaker by the end of the 21st century. *Geophys. Res. Lett.* **47** https://doi.org/10.1029/2020gl090441 (2020).
74. Woollings, T., Drouard, M., O'Reilly, C. H., Sexton, D. M. H. & McSweeney, C. Trends in the atmospheric jet streams are emerging in observations and could be linked to tropical warming. *Commun. Earth Environ.* **4** https://doi.org/10.1038/s43247-023-00792-8 (2023).
75. Vallis, G. K., Zurita-Gotor, P., Cairns, C. & Kidston, J. Response of the large-scale structure of the atmosphere to global warming. *Q. J. R. Meteorol. Soc.* **141**, 1479–1501 (2015).
76. Mann, H. B. Nonparametric tests against trend. *Econometrica* **13**, 245–259 (1945).
77. Hoskins, B. J. & Ambrizzi, T. Rossby wave propagation on a realistic longitudinally varying flow. *J. Atmos. Sci.* **50**, 1661–1671 (1993).
78. White, R. H., Kornhuber, K., Martius, O. & Wirth, V. From atmospheric waves to heatwaves: a waveguide perspective for understanding and predicting concurrent, persistent, and extreme extratropical weather. *Bull. Am. Meteorol. Soc.* **103**, E923–E935 (2022).
79. Holton, J. R. & Hakim, G. J. *An Introduction to Dynamic Meteorology*, Vol. 88 (Academic Press, 2013).
80. Simpson, I. R. et al. An evaluation of the large-scale atmospheric circulation and its variability in CESM2 and other CMIP models. *J. Geophys. Res. Atmos.* **125** https://doi.org/10.1029/2020jd032835 (2020).
81. Zhang, Y. et al. Disagreement in detected heatwave trends resulting from diagnostic methods. *Geophys. Res. Lett.* **52** https://doi.org/10.1029/2024gl114398 (2025).
82. Li, Z. & Ding, Q. A global poleward shift of atmospheric rivers. *Sci. Adv.* **10**, eadq0604 (2024).
83. Priestley, M. D. K. et al. An overview of the extratropical storm tracks in CMIP6 historical simulations. *J. Clim.* **33**, 6315–6343 (2020).
84. Delworth, T. L. et al. SPEAR: the next generation GFDL modeling system for seasonal to multidecadal prediction and projection. *J. Adv. Model. Earth Syst.* **12** https://doi.org/10.1029/2019ms001895 (2020).
85. Shevliakova, E. et al. The land component LM4.1 of the GFDL earth system model ESM4.1: model description and characteristics of land surface climate and carbon cycling in the historical simulation. *J. Adv. Model. Earth Syst.* **16** https://doi.org/10.1029/2023ms003922 (2024).
86. Lubis, S. W. et al. Enhanced Pacific Northwest heat extremes and wildfire risks induced by the boreal summer intraseasonal oscillation. *npj Clim. Atmos. Sci.* **7**, 232 (2024).
87. Xiang, B., Wang, B., Chen, G. & Delworth, T. L. Prediction of diverse boreal summer intraseasonal oscillation in the GFDL SPEAR model. *J. Clim.* **37**, 2217–2230 (2024).
88. Woollings, T. et al. Blocking and its response to climate change. *Curr. Clim. Change Rep.* **4**, 287–300 (2018).
89. Raymond, C., Matthews, T. & Horton, R. M. The emergence of heat and humidity too severe for human tolerance. *Sci. Adv.* **6**, eaaw1838 (2020).
90. Harnik, N., Messori, G., Caballero, R. & Feldstein, S. B. The Circumglobal North American wave pattern and its relation to cold events in eastern North America. *Geophys. Res. Lett.* **43** https://doi.org/10.1002/2016gl070760 (2016).
91. Riboldi, J., Leeding, R., Segalini, A. & Messori, G. MultiplE Large-scale Dynamical Pathways For Pan–Atlantic compound cold and windy extremes. *Geophys. Res. Lett.* **50** https://doi.org/10.1029/2022gl102528 (2023).
92. Lu, F. et al. GFDL's SPEAR seasonal prediction system: initialization and ocean tendency adjustment (OTA) for coupled model predictions. *J. Adv. Model. Earth Syst.* **12** https://doi.org/10.1029/2020ms002149 (2020).
93. Chen, M. et al. Assessing objective techniques for gauge-based analyses of global daily precipitation. *J. Geophys. Res.* **113** https://doi.org/10.1029/2007jd009132 (2008).
94. Guan, B. & Waliser, D. E. Detection of atmospheric rivers: evaluation and application of an algorithm for global studies. *J. Geophys. Res. Atmos.* **120**, 12514–12535 (2015).
95. Tseng, K. C. et al. Are multiseasonal forecasts of atmospheric rivers possible? *Geophys. Res. Lett.* **48** https://doi.org/10.1029/2021gl094000 (2021).
96. Clark, J. P., Johnson, N. C., Park, M., Bernardez, M. & Delworth, T. L. Predictable patterns of seasonal atmospheric river variability over North America during winter. *Geophys. Res. Lett.* **52** https://doi.org/10.1029/2024gl112411 (2025).
97. Mundhenk, B. D., Barnes, E. A. & Maloney, E. D. All-season climatology and variability of atmospheric river frequencies over the North Pacific. *J. Clim.* **29**, 4885–4903 (2016).
98. Park, M., Johnson, N. C., Hwang, J. & Jia, L. A hybrid approach for skillful multiseasonal prediction of winter North Pacific blocking. *npj Clim. Atmos. Sci.* **7** https://doi.org/10.1038/s41612-024-00767-2 (2024).
99. Sousa, P. M., Barriopedro, D., García-Herrera, R., Woollings, T. & Trigo, R. M. A new combined detection algorithm for blocking and subtropical ridges. *J. Clim.* **34**, 7735–7758 (2021).
100. McKenna, M. & Karamperidou, C. The impacts of El Niño diversity on Northern Hemisphere atmospheric blocking. *Geophys. Res. Lett.* **50** https://doi.org/10.1029/2023gl104284 (2023).

Acknowledgements

The authors thank Drs. Liwei Jia and Donghyuck Yoon for helpful comments on an earlier version of the manuscript. M.P. acknowledges funding under award NA18OAR4320123 and NA22OAR4050663D from the National Oceanic and Atmospheric Administration, U.S. Department of Commerce. The statements, findings, conclusions, and recommendations are those of the authors and do not necessarily reflect the views of the National Oceanic and Atmospheric Administration or the U.S. Department of Commerce.

Author contributions

M.P. conceived the study, conducted the analysis, and drafted the manuscript. N.C.J. contributed to the interpretation of the results, provided critical feedback throughout the development of the project, and participated in writing the manuscript.

Competing interests

The authors declare no competing interests.

Additional information

Supplementary information The online version contains supplementary material available at https://doi.org/10.1038/s41612-025-01319-y.

Correspondence and requests for materials should be addressed to Mingyu Park.

Reprints and permissions information is available at http://www.nature.com/reprints

Publisher's note Springer Nature remains neutral with regard to jurisdictional claims in published maps and institutional affiliations.

Open Access This article is licensed under a Creative Commons Attribution-NonCommercial-NoDerivatives 4.0 International License, which permits any non-commercial use, sharing, distribution and reproduction in any medium or format, as long as you give appropriate credit to the original author(s) and the source, provide a link to the Creative Commons licence, and indicate if you modified the licensed material. You do not have permission under this licence to share adapted material derived from this article or parts of it. The images or other third party material in this article are included in the article's Creative Commons licence, unless indicated otherwise in a credit line to the material. If material is not included in the article's Creative Commons licence and your intended use is not permitted by statutory regulation or exceeds the permitted use, you will need to obtain permission directly from the copyright holder. To view a copy of this licence, visit http://creativecommons.org/licenses/by-nc-nd/4.0/.

© The Author(s) 2026